Chemical abundances in Seyfert galaxies – VII. Direct abundance determination of neon based on optical and infrared emission lines

Mark Armah,[1,2]* O. L. Dors,[1]† C. P. Aydar,[3] M. V. Cardaci,[4,5] G. F. Hägele,[4,5] Anna Feltre,[6,7] R. Riffel,[2] R. A. Riffel[8] and A. C. Krabbe[1]

[1] *Universidade do Vale do Paraíba. Av. Shishima Hifumi, 2911, CEP: 12244-000, São José dos Campos, SP, Brazil*
[2] *Departamento de Astronomia, Universidade Federal do Rio Grande do Sul, Av. Bento Gonçalves 9500, Porto Alegre, RS, Brazil*
[3] *Universidade de São Paulo. R. do Matão, 1226, CEP: 05508-090, São Paulo, SP, Brazil*
[4] *Instituto de Astrofísica de La Plata (CONICET-UNLP), Argentina*
[5] *Facultad de Ciencias Astronómicas y Geofísicas, Universidad Nacional de La Plata, Paseo del Bosque s/n, 1900 La Plata, Argentina*
[6] *SISSA, Via Bonomea 265, 34136 Trieste, Italy*
[7] *INAF - Osservatorio di Astrofisica e Scienza dello Spazio di Bologna, Via P. Gobetti 93/3, 40129 Bologna, Italy*
[8] *Departamento de Física, Centro de Ciências Naturais e Exatas, Universidade Federal de Santa Maria, 97105-900, Santa Maria, RS, Brazil*

ABSTRACT

For the first time, neon abundance has been derived in the narrow line region from a sample of Seyfert 2 nuclei. In view of this, we compiled from the literature fluxes of optical and infrared (IR) narrow emission lines for 35 Seyfert 2 nuclei in the local universe ($z \lesssim 0.06$). The relative intensities of emission lines were used to derive the ionic and total neon and oxygen abundances through electron temperature estimations (T_e-method). For the neon, abundance estimates were obtained by using both T_e-method and IR-method. Based on photoionization model results, we found a lower electron temperature $[t_e(\text{Ne\,III})]$ for the gas phase where the Ne^{2+} is located in comparison with t_3 for the O^{2+} ion. We find that the differences (D) between $\text{Ne}^{2+}/\text{H}^+$ ionic abundances calculated from IR-method and T_e-method (assuming t_3 in the $\text{Ne}^{2+}/\text{H}^+$ derivation) are similar to the derivations in star-forming regions (SFs) and they are reduced by a mean factor of ~ 3 when $t_e(\text{Ne\,III})$ is considered. We propose a semi-empirical Ionization Correction Factor (ICF) for the neon, based on [Ne\,II]12.81μm, [Ne\,III]15.56μm and oxygen ionic abundance ratios. We find that the average Ne/H abundance for the Seyfert 2s sample is nearly 2 times higher than similar estimate for SFs. Finally, for the very high metallicity regime (i.e. $[12 + \log(\text{O/H}) \gtrsim 8.80]$) an increase in Ne/O with O/H is found, which likely indicates secondary stellar production for the neon.

Key words: galaxies: active – galaxies: abundances – galaxies: evolution – galaxies: nuclei – galaxies: ISM – galaxies: Seyfert –ISM: abundances

1 INTRODUCTION

Active Galactic Nuclei (AGNs) present prominent emission lines in their spectra, whose relative intensities can be used to estimate the metallicity and elemental abundances of heavy elements (O, N, Ne, S, etc.) in the gas-phase of these objects. This feature, together with their high luminosity, has made these objects essential to chemical evolution studies of galaxies along the Hubble time.

The first chemical abundance study in AGNs, based on direct determination of the electron temperature (hereafter T_e-method), was carried out by Osterbrock & Miller (1975) for the radio galaxy 3C 405 (Cygnus A). These authors derived the oxygen abundance relative to hydrogen (O/H) (among other elements) in the order of 12+log(O/H)=8.60. Most AGN studies have mainly been carried out following this aforementioned pioneering work. In fact, Ferland & Netzer (1983) compared observational optical emission line ra-

* E-mail: armah@ufrgs.br
† E-mail: olidors@univap.br

tios to photoionization model predictions built with the first version of the CLOUDY code (Ferland & Truran 1980) and found that the metallicities of Seyfert 2s are in the range $0.1 \lesssim (Z/Z_\odot) \lesssim 1$, but the nitrogen abundance can have a relative enhancement in relation with oxygen, which is analogous to H II regions. Thereafter, several studies have relied on the estimations of metallicities for AGNs using photoionization models in the local universe (e.g. Stasińska 1984; Ferland & Osterbrock 1986; Storchi-Bergmann et al. 1998; Groves et al. 2006; Feltre et al. 2016; Castro et al. 2017; Pérez-Montero et al. 2019; Thomas et al. 2019; Carvalho et al. 2020) as well as at high redshifts (e.g. Nagao et al. 2006; Matsuoka et al. 2009, 2018; Nakajima et al. 2018; Dors et al. 2014, 2018, 2019; Mignoli et al. 2019; Guo et al. 2020).

Since oxygen presents prominent emission lines (e.g. [O II]λ3726 Å+λ3729 Å, [O III]λ4959, λ5007 Å) in the optical spectrum of gaseous nebulae, emitted by its most abundant ions (O^+, O^{2+}), it has usually been used as metallicity tracer for the gas phase of line-emitting objects (e.g. Dors 2021; Kewley et al. 2019). Specifically, Flury & Moran (2020) and Dors et al. (2020c) found that the O^{3+} abundance in AGNs is not larger than 20 per cent of the total O/H abundance. Therefore, the oxygen abundance determination has usually been derived through only the lines emitted by O^+ and O^{2+} ions (for a review, see Dors et al. 2020b). On the other hand, the abundances of other heavy elements, e.g. N, Ne, S, etc., are poorly known in AGNs. Dors et al. (2017) presented the first quantitative nitrogen abundance determination for a sample of 44 Seyfert 2 nuclei in the local universe ($z \lesssim 0.1$; see also Contini 2017; Pérez-Montero et al. 2019). Moreover, for the sulphur, only qualitative abundance determinations, based on the comparison between observational line ratios and photoionization model predictions were performed by Storchi-Bergmann & Pastoriza (1990).

In galaxy evolution and stellar nucleosynthesis, the knowledge of neon abundance is relevant, especially among the heavy elements. Neon is one of the noble gas elements which does not combine with itself or with other chemical species in the formation of molecules and dust grains (e.g. Jenkins 1987; Henry 1993; Sofia et al. 1994; Sofia 2004; Brinchmann et al. 2013). Therefore, the depletion of abundance in the gas phase process is not expected in neon, conversely to such occurrence in the oxygen (e.g. Izotov et al. 2006; Pilyugin et al. 2007) and refractory elements (e.g. Mg, Si, Fe; Osterbrock et al. 1992; Peimbert et al. 1992, 1993; Garnett et al. 1995; Peimbert & Peimbert 2010) trapped in dust. Regarding chemical galaxy evolution, the chemical abundances of neon and oxygen are expected to closely trace each other (Crockett et al. 2006) due to the fact that both elements are produced in stars more massive than 10 M$_\odot$ (e.g. Woosley & Weaver 1995) and a constant Ne/O abundance ratio over a wide range of O/H abundance is supposed to be found. However, chemical abundance studies of star-forming regions have revealed a slight dependence of Ne/O on O/H (see Dors et al. 2013 and references therein), which brings forth a worthwhile means of cross-checking the stellar nucleosynthesis theory.

The study of neon and oxygen abundances in AGNs can also provide important insights into the origin of heavy elements, mainly in the regime of high metallicities. Unfortunately, neon abundance in relation with hydrogen (Ne/H) in

AGNs is rarely found in the literature, and only a few AGNs relative abundance of Ne with other heavy elements has been derived. For instance, Nussbaumer & Osterbrock (1970), by using the T_e-method, derived the Fe/Ne abundance ratio for NGC 4151 to be 0.11. Assuming a solar abundance ratio (Fe/Ne)$_\odot$ = 0.282 (Holweger 2001) shows that AGNs have an overabundance of Fe, as found by Hamann & Ferland (1993). The above result indicates a very high and oversolar neon abundance. Furthermore, based on a comparison between observational soft X-ray spectrum of the Narrow Line Quasar PG1404+226 ($z = 0.098$) and photoionization model predictions, Ulrich et al. (1999) found that the abundances of oxygen and neon are about 0.2 and 4 times the solar value, respectively, which again implies an overabundance value of neon. However, Shields et al. (2010), who compared AGNs spectra from the Sloan Digital Sky Survey (SDSS, York et al. 2000) in the redshift range of $0.2 < z < 0.35$ with photoionization model predictions, found no significant difference for the Fe/Ne abundance ratios in the sample of objects considered.

With the foregoing in mind, the primary aim of this study is to derive neon abundance in relation with hydrogen (Ne/H) in the NLRs of relatively large sample of Seyfert 2s at low redshift ($z \lesssim 0.06$) and compare the results with previous SFs findings. In view of this, we compiled from the literature narrow optical and infrared (IR) emission line intensities for Seyfert 2 galaxies. These observational data will be used to derive the twice ionized (Ne^{2+}/H^+) and total (Ne/H and O/H) abundances through the T_e-method and infrared emission lines method. Also, it is possible to derive the singly ionized neon abundance relative to hydrogen (Ne^+/H^+) through infrared emission lines. The use of T_e-method, based on direct temperature determinations via optical lines (for a review see Peimbert et al. 2017; Pérez-Montero 2017) can lead to non-negligible deviations in the estimations of abundances, in the sense that abundances can be underestimated in relation with other distinct methods. Therefore, we also consider Ne/H abundances derived from IR lines, which have weak dependence on the electron temperature (Simpson 1975).

This paper is organized as follows. In Section 2, we describe the observational data. In Sect. 3 details to the calculations of the ionic abundances from T_e-method and infrared emission lines are presented. Descriptions of the calculation of the total neon and oxygen abundances are given in Sect. 4. The results and discussions are presented in Sect. 5 and Sect. 6, respectively. Finally, we summarize our conclusions in Sect. 7.

2 OBSERVATIONAL DATA

In order to study the Ne^{+2}/H^+ abundances we take into account the fact that Dors et al. (2013) found Ne^{2+}/H^+ abundance estimations in H II regions using the T_e-method are lower by a factor of ~ 4 than those obtained through infrared lines, which are less sensitive to electron temperature. Therefore, we consider AGN emission lines measured in both wavelength ranges in order to ascertain if similar discrepancy exists in AGNs. The caveat here is that it is unknown which among the T_e- and IR-methods provides more accurate abundance values.

We limit the abundance determinations to the NLRs of Seyfert 2s because shocks with low velocity (lower than 400 km s^{-1}, Contini 2017; Dors et al. 2020a) are expected in this type of object and the T_e-method was adapted for this object type in a previous paper (Dors et al. 2020c). The selection criteria for the objects are:

(i) The objects must be classified as Seyfert 2 nuclei.

(ii) They must have the narrow optical [O II]λ3726 + λ3729, [Ne III]λ3869, [O III]λ4363, Hβ, [O III]λ5007, Hα and [S II]λ6716, λ6731 emission-line fluxes measured.

(iii) The [Ne III]λ15.56 μm emission-line fluxes should also be measured. The flux of the [Ne II]12.81μm line is considered in the compiled data when it is available in the original work.

The optical data consists of emission lines observed in the wavelength range of 3500 < λ(Å) < 8000 obtained with

(i) low-dispersion spectra ($R \sim 5 - 10$ Å) using telescopes at the Las Campanas, Anglo-Australian, Lick and European Southern observatories and

(ii) Faint Object Spectrograph spectroscopy (FOS) on board the Hubble Space Telescope (HST) at 3500 < λ (Å) < 7000 ($R \sim 5$ Å).

The infrared observational data from near to mid infrared spectroscopic observations were obtained from the following:

(i) Photodetector Array Camera and Spectrometer (PACS) instrument on board the European Space Agency (ESA) Herschel Space Observatory in the short cross-dispersed mode ($R \sim 360$) covering the $JHK-$bands, together with an ancillary data,

(ii) *Spitzer*−Infrared Spectrometer (IRS) spectroscopic survey consisting of the short wavelengths ranging from 9.9 to 19.6 μm covered by the Short-High (SH) module in the high spectral resolution mode ($R \sim 600$) and from 8 to 2.4 μm,

(iii) medium resolution ($R \sim 1500$) of Infrared Space Observatory Short Wavelength Spectrometer (ISO-SWS) 2.4 − 45 μm spectra,

(iv) the cooled grating spectrometer 4 (CGS4) on United Kingdom Infrared Telescope (UKIRT) for both high-resolution ($R = 1260$) and low-resolution ($R = 345$ and 425) $JHK-$band spectra of 4 μm spectroscopy with ISAAC at the European Southern Observatory Very Large Telescope array (ESO VLT),

(v) Infrared array spectrometer - IRSPEC ($R \sim 1500$) at the ESO 3.6 m telescope,

(vi) Infrared Spectrometer And Array Camera Long Wavelength (ISAAC-LW) medium resolution spectroscopy mode covering a range of 3.93 to 4.17 μm at spectral resolving power ~ 2500,

(vii) Anglo-Australian Telescope NIR integral field spectroscopy of moderate resolution ($R \sim 2100$) $KL-$bands spectra from 2.17 - 2.43μm, and

(viii) H (1.5 - 1.8 μm) and K (2.0 - 2.4 μm) bands corresponding to the spectral resolutions $\lambda/\Delta\lambda = 1700$ and $\lambda/\Delta\lambda = 1570$, respectively, using the Keck NIR longslit spectrograph NIRSPEC.

In Tables A1 and A2, available as supplementary material, the objects identifications, the optical and infrared

observational emission line fluxes and the bibliographic references to the origins of the data are listed.

The observational data considered in this work consist of a heterogeneous sample, thus, the data were obtained with different instrumentation and observational techniques with different apertures, which could potentially introduce some uncertainties in the derivation of physical properties for the objects under consideration. Dors et al. (2013) analysed these effects on oxygen abundance determinations in star-forming regions and did not find any bias in the physical conditions of the objects obtained by using a similarly heterogeneous samples. A particular concern in AGN studies is the emission contribution from H II regions to the measured AGN flux, which can be located at few parsecs away from the AGN (e.g. Boer & Schulz 1993; Elmegreen et al. 2002; Díaz et al. 2007; Dors et al. 2008; Böker et al. 2008; Riffel et al. 2009; Hägele et al. 2013; Álvarez-Álvarez et al. 2015; Riffel et al. 2016; Dametto et al. 2019). In fact, Thomas et al. (2018a), who considered a large sample of AGNs data taken from the Sloan Digital Sky Survey (SDSS, York et al. 2000), found that, even for strong AGNs [with log([O III]λ5007/Hβ) $\gtrsim$ 0.9], $\sim$ 30 per cent of the Balmer line fluxes, on average, is emitted by H II regions (see also Davies et al. 2014a,b; D'Agostino et al. 2018, 2019; Thomas et al. 2018b).

Dors et al. (2020b) investigated the aperture effect on oxygen abundance and electron density estimates in a sample of local AGNs ($z \lesssim 0.4$) using SDSS spectra (York et al. 2000), which were obtained with a fixed diameter of the fibres of $\sim$ 3 arcsec. Since H II regions generally have lower O/H abundances (e.g. Kennicutt et al. 2003; Groves et al. 2006) and electron density values (e.g. Copetti et al. 2000; Dors et al. 2014) than similar estimations in AGNs, if the emission from H II regions contributes significantly to the observed emission-line fluxes in AGNs, a decrease in O/H and N_e with increasing redshift (a greater number of H II regions were included within the fiber at larger distances) would be expected. However, no correlation between O/H or N_e with the redshift was derived by these authors, indicating negligible aperture effects on the AGN parameter estimations. Moreover, Kewley et al. (2005) found that the derived metallicity can vary by a factor of only 0.14 dex from the value obtained when the fluxes are measured with the assumption of an aperture capturing less than 20 per cent of the total emissions from a galaxy. The object of our sample with the highest redshift is Cygnus A ($z = 0.05607$), where assuming a spatially flat cosmology with the present-day Hubble parameter being $H_0 = 71$ km s^{-1}Mpc^{-1}, the total present matter density $\Omega_m = 0.270$, the total present vacuum density $\Omega_{\rm vac} = 0.730$ (Wright 2006) and a typical aperture of 2 arcsec, corresponds to a physical scale in the center of this galaxy of about 2 kpc, i.e. the emissions are mainly from an AGN.

In Figure 1 we show plots for Paβ and Brγ versus all other strong Paschen and Brackett line series samples of our IR observational data compiled from the literature (i.e. taken from Moorwood & Oliva 1988; Kawara et al. 1989; Oliva et al. 1994; Goldader et al. 1995, 1997; Veilleux et al. 1997, 1999; Bryant & Hunstead 1999; Gilli et al. 2000; Winge et al. 2000; Lutz et al. 2002; Reunanen et al. 2002; Sturm et al. 2002; Rodríguez-Ardila et al. 2005; Riffel et al. 2006; Ramos Almeida et al. 2009; Onori et al. 2017) which have

strong Paschen and Brackett line series corresponding to Paβ and Brγ. It can be seen from Fig. 1 that the IR H I line fluxes have a clear linear correlation for all the strong emission lines with somewhat scattering in the points, which is probably due to the heterogeneity of the sample. However, we show (see below) that abundance estimates assuming different IR H I lines have a very good agreement with each other, therefore, this observed scatter in Fig. 1 has no effect on our abundance results. Since most of the observed hydrogen recombination lines have been reddening-corrected by the original authors and the infrared line series show little deviations with Paβ and Brγ, we considered them in our abundance estimations without further consideration for extinction correction.

2.1 Diagnostic diagrams

Although the objects in our sample have been classified as AGNs by the authors from which the data were compiled, we produced an additional test based on standard Baldwin-Phillips-Terlevich (BPT) diagrams (Baldwin et al. 1981; Veilleux & Osterbrock 1987). These diagnostic diagrams, based on optical emission-line ratios, have been used to distinguish objects whose main ionization mechanisms are massive stars from those that are mainly ionized by AGNs and/or gas shocks (see also Kewley et al. 2001, 2013; Kauffmann et al. 2003; Pérez-Montero et al. 2013; Ji & Yan 2020). We adopted the criteria proposed by Kewley et al. (2001) where all objects with

$$\log([\text{O III}]\lambda 5007/\text{H}\beta) > \frac{0.61}{[\log([\text{N II}]\lambda 6584/\text{H}\alpha) - 0.47]} + 1.19,$$
(1)

$$\log([\text{O III}]\lambda 5007/\text{H}\beta) > \frac{0.72}{[\log([\text{S II}]\lambda 6725/\text{H}\alpha) - 0.32]} + 1.30$$
(2)

and

$$\log([\text{O III}]\lambda 5007/\text{H}\beta) > \frac{0.73}{[\log([\text{O I}]\lambda 6300/\text{H}\alpha) + 0.59]} + 1.33$$
(3)

have AGNs as their main ionization mechanism. The [S II]λ6725 line above represents the sum of the [S II]λ6717 and [S II]λ6731 lines. Fig. 2 further confirms that the ionizing sources of the objects in our sample are indeed AGNs. Additionally, it can be seen that the objects cover a large range of ionization degree and metallicity since a wide range of [O III]/Hβ and [N II]/Hα are observed (e.g. Feltre et al. 2016; Agostino et al. 2021).

2.2 Reddening correction

We performed the reddening correction to the optical emission lines by considering the expression

$$\frac{I(\lambda)}{I(\text{H}\beta)} = \frac{F(\lambda)}{F(\text{H}\beta)} \times 10^{c(\text{H}\beta)[f(\lambda) - f(\text{H}\beta)]},$$
(4)

where $I(\lambda)$ is the intensity (reddening corrected) of the emission line at a given wavelength λ, $F(\lambda)$ is the observed flux
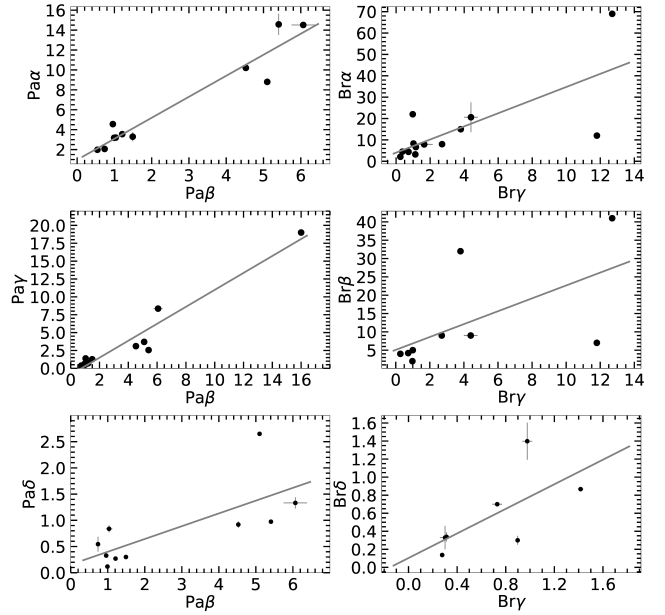

Figure 1. Strong IR emission line (in units of 10^{-14} erg cm^{-2} s^{-1}) ratios for each spectra in our sample for which the Paschen and Brackett series were detected. Left-column: plots for the measured Paβ line flux versus measured Paα, Paγ and Paδ. Right-column: plots for the measured Brγ line flux versus other measured Brackett series (Brα, Brβ and Brδ).

of the emission line, $f(\lambda)$ is the adopted reddening curve normalized to Hβ and $c(\text{H}\beta)$ is the interstellar extinction coefficient. The extinction coefficient of interest is normally calculated using the Hα/Hβ line ratio and comparing it with its theoretical value. For instance, the estimation by Hummer & Storey (1987) for a temperature of 10 000 K and an electron density of 100 cm^{-3} produces $I(\text{H}\alpha/\text{H}\beta) = 2.86$. Following the parameterization by Whitford (1958), adopting the reddening curve by Miller & Mathews (1972) and using a consensual assumed value of the ratio of total to selective absorption in the optical V band, with $R_V = 3.1$, for the diffuse interstellar medium (see Cardelli et al. 1989; O'Donnell 1994; Fitzpatrick 1999, and references therein), we deduce the logarithmic extinction at Hβ expressed as

$$c(\text{H}\beta) = 3.10 \times \left[\log\left(\frac{F(\text{H}\alpha)}{F(\text{H}\beta)} \right) - \log\left(\frac{I(\text{H}\alpha)}{I(\text{H}\beta)} \right) \right].$$
(5)

The optical extinction curves in the extragalactic environment are closely parallel to those of the Milky Way in all related extinction studies, with R_V values comparable to the canonical value of 3.1 (e.g. McCall 2004; Finkelman et al. 2008).

In comparison with the Case B recombination value of 2.86, Halpern (1982) and Halpern & Steiner (1983), adopting photoionization models, found that $I(\text{H}\alpha/\text{H}\beta)$ is close to 3.10 in AGNs with high and low ionization degree. This contradicts Heckman (1980) preposition of an anomalously high Balmer decrement in these objects. Therefore, $I(\text{H}\alpha/\text{H}\beta) = 2.86$ and 3.10 intrinsic ratios are usually considered to be estimations for H II regions and AGNs, respectively (Ferland & Netzer 1983; Gaskell 1982, 1984; Gaskell & Ferland 1984; Veilleux & Osterbrock 1987; Wysota & Gaskell 1988). Par-
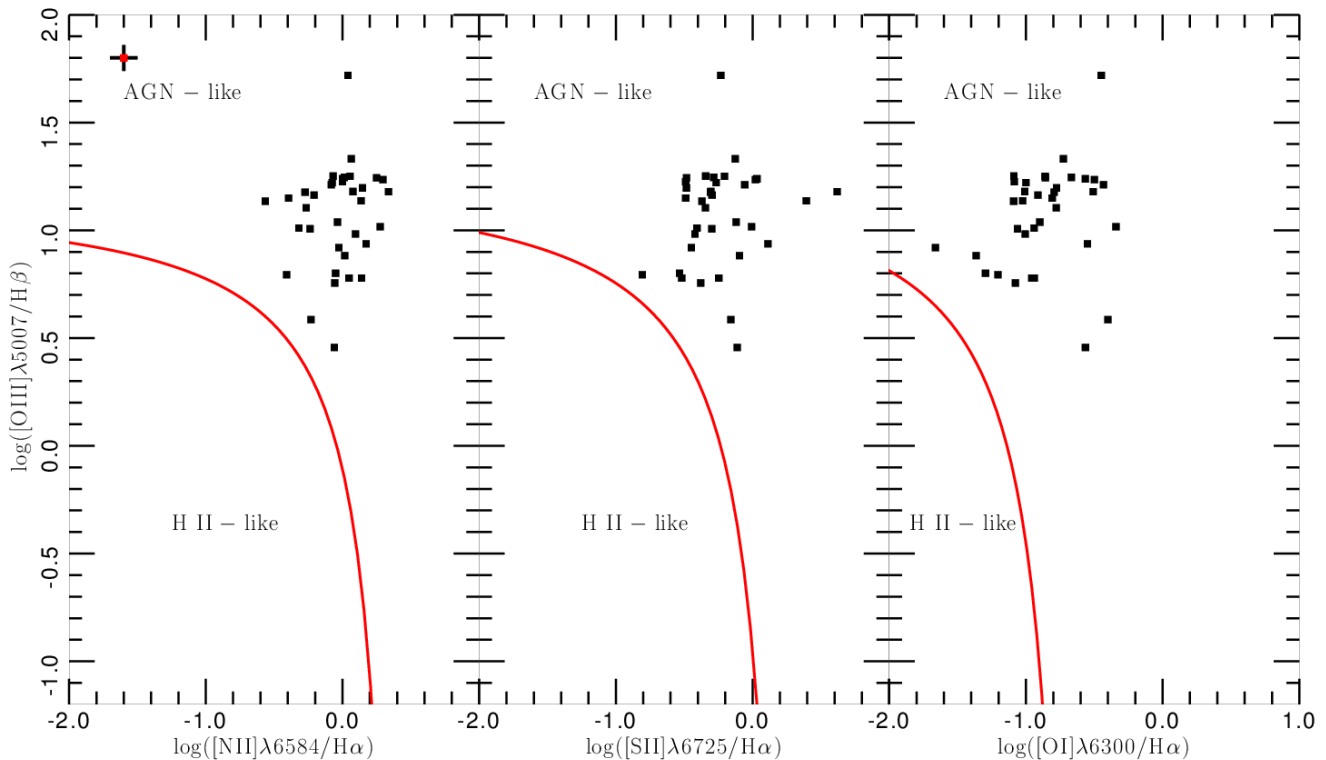
Figure 2. Diagnostic diagrams for emission-line ratios of $\log([\text{O\,III}]\lambda5007/\text{H}\beta)$ versus $\log([\text{N\,II}]\lambda6584/\text{H}\alpha)$, $\log([\text{S\,II}](\lambda6725)/\text{H}\alpha)$, and $\log([\text{O\,I}](\lambda6300)/\text{H}\alpha)$. $[\text{S\,II}]\lambda6725$ represents the sum of the lines $[\text{S\,II}]\lambda6717$ and $[\text{S\,II}]\lambda6731$. Points represent objects of our sample (see Sect. 2). Red lines, by Kewley et al. (2001) and represented by Eqs. 1, 2 and 3, separate objects ionized by massive stars from those ionized by gas shocks and/or AGN-like objects, as indicated. Error bar, in left panel, represents the typical uncertainty (0.1 dex) in emission-line ratio measurements (e.g. Kraemer et al. 1994).

ticularly, in AGNs, there is a large transition zone, or partly ionized region, in which H^0 coexists with H^+ and free electrons. In this zone, collisional excitation is also important in addition to recombination (Ferland & Netzer 1983; Halpern & Steiner 1983). The main effect of collisional excitation is to enhance $\text{H}\alpha$. The higher Balmer lines are less affected because of their large re-excitation energies and smaller excitation cross-sections.

In order to check the $\text{H}\alpha/\text{H}\beta$ value assumed in our reddening correction, we consider results from AGNs photoionization models built with the CLOUDY code (Ferland et al. 2013) by Carvalho et al. (2020). This grid of models assume a wide range of nebular parameters, i.e. a Spectral Energy Distribution with power law $\alpha_{ox} = -0.8, -1.1, -1.4$, oxygen abundances in the range of $8.0 \leqq 12 + \log(\text{O/H}) \leqq 9.0$, logarithm of the ionization parameter (U) in the range of $-4.0 \leqq \log U \leqq -0.5$, and electron density $N_e = 100, 500$ and 3000 cm^{-3}. The AGN parameters considered in the models built by Carvalho et al. (2020) cover practically all the range of physical properties of a large sample of Seyfert 2 nuclei. We excluded models with $\alpha_{ox} = -1.4$ and $\log U = -4.0$ because they predicted emission lines which are not consistent with observational data (see Pérez-Montero et al. 2019; Carvalho et al. 2020). The Carvalho et al. (2020) models assume constant electron density along the nebular radius while spatially resolved studies of AGNs have found N_e variations from ~ 100 to $\sim 3000 \text{ cm}^{-3}$ along the NLRs of some

AGNs (e.g. Freitas et al. 2018; Kakkad et al. 2018; Mingozzi et al. 2019; Riffel et al. 2021a). However, to provide a simple test for this problem, Dors et al. (2019) built AGN photoionization models assuming a profile density similar to observational estimations by Revalski et al. (2018a) in the Seyfert 2 Mrk 573, i.e. with a central electron density peak at $\sim 3000 \text{ cm}^{-3}$ and a decrease in this value following a shallow power law. Dors et al. (2019) found that predicted emission lines assuming this density profile are very similar to those considering a constant electron density along the AGN radius. Therefore, N_e variations have almost a negligible effect on emission lines and abundances predicted by photoionization models, at least for the low electron density limit ($\lesssim 10^4 \text{ cm}^{-3}$).

In Fig. 3, bottom panel, we show the model predictions of the gas ionization degree parameterized by the $[\text{O\,III}]\lambda5007/[\text{O\,II}]\lambda3727$ line ratio versus $\text{H}\alpha/\text{H}\beta$ ratio. In this figure, the expected values for the $\text{H}\alpha/\text{H}\beta$ ratio, considering the theoretical values by Storey & Hummer (1995) for different temperature values of 5000 K, 10 000 K and 20 000 K are indicated by the solid black lines representing 3.10, 2.86 and 2.69, respectively. We notice that most of the models ($\sim95\,\%$) predict $\text{H}\alpha/\text{H}\beta$ values in the range from 2.69 to 3.10. In Fig. 3, top panel, the distribution of $\text{H}\alpha/\text{H}\beta$ values predicted by the models is shown, where it can be seen that, the most representative value is around $(\text{H}\alpha/\text{H}\beta)=2.90$ with an average value of 2.89 ± 0.22. Therefore, for the intrinsic
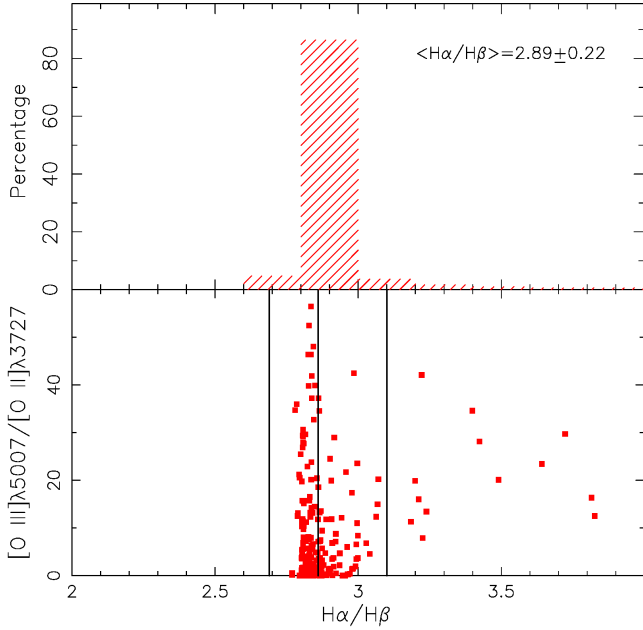
Figure 3. Bottom panel: [O III]λ5007/[O II]λ5007 versus Hα/Hβ. The red points represent AGN photoionization model predictions taken from Carvalho et al. (2020). The black lines represent the theoretical values from Storey & Hummer (1995) for temperatures of 5000 K (3.10), 10 000 K (2.86) and 20 000 K (2.69). Top panel: Distribution of Hα/Hβ values. The average for the Hα/Hβ values is indicated.

ratio of Seyfert 2 nuclei, we adopted the theoretical value given by (Hα/Hβ)=2.86.

The wavelength dependence in the optical domain, $f(\lambda)$, is the reddening value for the line derived from the curve given by Whitford (1958), which is defined such that $f(\infty) = -1$ and $f(\text{H}\beta) = 0$. An analytical expression for the estimation of $f(\lambda)$ following the proposal by Kaler (1976) was used in the derivation of the extinction curve, which is given by:

$$f(\lambda) = 2.5659\lambda^2 - 4.8545\lambda + 1.7545, \qquad (6)$$

with λ in units of micrometers within the range $0.35 \lesssim \lambda(\mu m) \lesssim 0.70$. We adopted negligible intrinsic reddening when the apparent Balmer decrement from the original work is $\lesssim 2.86$ and the extinction correction constant indicates a value of zero as shown in Table A3, thus, $c(\text{H}\beta) = 0.0$

Since several measurements for the emission lines compiled from the literature do not have their errors listed in the original papers where the data were compiled, we adopted a typical error of 10% for strong emission-lines (e.g. [O III]λ5007) and 20 % for weak emission lines, in the case of [O III]λ4363 (see, for instance, Kraemer et al. 1994; Hägele et al. 2008). These errors were used to calculate the uncertainties in the derived values of electron temperatures (in order of 800 K) and abundances (in order of 0.1 dex).

3   IONIC ABUNDANCE DETERMINATIONS

The main goal of this work is to estimate the total abundance of neon in relation with hydrogen (Ne/H) for the

NLRs of a sample of Seyfert 2 objects. This can be carried out by using optical and infrared emission lines. In view of this, for optical lines, we adopted the T_e-method used by Dors et al. (2020c) to be applied in the studies of Seyfert 2 nuclei. Regarding abundances obtained through infrared lines, the methodology proposed by Dors et al. (2013) was adopted in this work, which is based on Petrosian (1970), Simpson (1975), Förster Schreiber et al. (2001), and Vermeij & van der Hulst (2002).

The observational optical data compiled from the literature make it possible to estimate only the Ne^{2+}/H$^+$ ionic abundance. Therefore, to obtain Ne/H, Ionization Correction Factors (ICFs) based on the neon infrared lines and photoionization models were employed. The O/H abundance for our sample was calculated by using only the T_e-method, since there are few emission lines of this element measured in the infrared wavelength range under consideration (e.g. van Loon et al. 2010). In the succeeding subsections, each of the adopted methodology in the estimations of the Ne and O abundances is succinctly described.

3.1 T_e-method

In determining ionic abundances using the T_e-method, basically, it is necessary to obtain measurements of the intensity of the emission lines emitted by the ions under consideration and the representative values of the electron temperature (T_e) and electron density (N_e) of the gas region where these ions are located (Osterbrock 1989).

Hägele et al. (2008) obtained, from the task TEMDEN of IRAF[1] (De Robertis et al. 1987; Shaw & Dufour 1995), functions to determine electron temperatures. It is considered that t_3 and t_2 are the electron temperatures (in units of 10^4 K) for the electrons that are exciting the O^{2+} and O$^+$ ions in the high and low ionization zones, respectively. The expressions obtained by Hägele et al. (2008) were assumed to calculate t_3, O^{2+}/H$^+$, O$^+$/H$^+$ and Ne^{2+}/H$^+$.

First, for each object in our sample, the electron temperature in the high-ionization zone (t_3) was obtained by using the expression

$$t_3 = 0.8254 - 0.0002415 \times R_{O3} + \frac{47.77}{R_{O3}}, \qquad (7)$$

where $R_{O3} = $ [O III]$(\lambda 4959\text{Å} + \lambda 5007\text{Å})/\lambda 4363\text{Å}$. This relation is valid for a range $30 \lesssim R_{O3} \lesssim 700$, corresponding to a temperature range of $0.7 \lesssim t_3 \lesssim 2.3$. Only objects with t_3 in this range of values were considered in the present analysis.

Consequently, it is not possible to explicitly estimate t_2 in the AGN spectra of our sample where the [O II]λ3727Å/λ7325Å emission line ratio can not be measured. Thus, we assumed the t_2-t_3 relation derived by Dors et al. (2020c) from a grid of photoionization models built using the CLOUDY code (Ferland et al. 2013). The theoretical resulting relation is given by

$$t_2 = (\text{a} \times t_3^3) + (\text{b} \times t_3^2) + (\text{c} \times t_3) + \text{d}, \qquad (8)$$

---

[1] Image Reduction and Analysis Facility (IRAF) is distributed by the National Optical Astronomy Observatories, which are operated by the Association of Universities for Research in Astronomy, Inc., under cooperative agreement with the National Science Foundation.

where a $= 0.17$, b $= -1.07$, c $= 2.07$ and d $= -0.33$.

The t_3-t_2 relation for SFs has issue of some uncertainties due to the large scatter between these temperatures, around 900 K (e.g. Berg et al. 2020) and this problem has been addressed in several chemical abundance studies. For example, Hägele et al. (2008) pointed out that the scatter in the t_3-t_2 relation can be due to electron density effects because the [O II] temperature is somewhat dependent on the density. Curti et al. (2017) pointed out that the [O III]$\lambda 4363$ can be contaminated by the neighboring [Fe II]$\lambda 4360$ line, mainly for objects with high metallicity $(12 + \log(O/H) \gtrsim 8.4)$. Recently, Arellano-Córdova & Rodríguez (2020) showed that the t_3 and $t_e(N II)$ ($\approx t_2$) relation depends on the ionization degree of the gas phase in SFs. In fact, the model results adopted to derive Eq. 8 by Dors et al. (2020c) also present a large scatter, which is not explained by electron density effects. However, Riffel et al. (2021a) showed that the relation given by Eq. 8 is in consonance with direct estimates of temperature for AGNs when no clear gas outflows are present in these objects. Unfortunately, direct estimates of t_2 for AGNs are rare in the literature and we stress that the use of Eq. 8 can yield somewhat uncertain in O^+ temperature estimates.

We make use of the relations to estimate ionic abundance of the singly and doubly ionized oxygen originally derived by Pagel et al. (1992) and in its current form given by Hägele et al. (2008) as:

$$12 + \log\left(\frac{O^{2+}}{H^+}\right) = \log\left(\frac{I(4959\,\text{Å}) + I(5007\,\text{Å})}{I(H\beta)}\right) + 6.144$$

$$+ \frac{1.251}{t_3} - 0.55 \times \log t_3$$

(9)

and

$$12 + \log\left(\frac{O^+}{H^+}\right) = \log\left(\frac{I(3727\,\text{Å})}{I(H\beta)}\right) + 5.992 + \frac{1.583}{t_2}$$

$$- 0.681 \times \log t_2 + \log[1 + 2.3 n_e]$$

(10)

where $n_e = 10^{-4} \times N_e$.

The electron density N_e for each object was derived through the relation of this parameter with the line ratio [S II]$\lambda 6717$/[S II]$\lambda 6731$ by using the IRAF code (Tody 1986; De Robertis et al. 1987; Shaw & Dufour 1995) and assuming the t_2 value obtained for each object. We derived electron density values in the range of $300 \lesssim N_e(\text{cm}^{-3}) \lesssim 3\,500$, with an average value of $\sim 1\,000\,\text{cm}^{-3}$. In Dors et al. (2020c), a detailed analysis of the effect of the electron density on the direct abundance determination was presented and it is not repeated here. We only point out to the fact that, despite high N_e values in order of 13 000 - 80 000 cm^{-3} derived when optical lines emitted by ions with higher ionization potential than the S^+ are used to derive the electron density, e.g. [Ar IV]$\lambda 4711$/$\lambda 4740$ line ratio (see Congiu et al. 2017; Riffel et al. 2021a), these values are much lower than the critical densities (e.g. see Vaona et al. 2012) for the optical lines used here. Additionally, the electron density determined from the

line ratio [S II]$\lambda 6717$/[S II]$\lambda 6731$ is much lower than that obtained using auroral and transauroral lines, as well as ionization parameter based approach (Davies et al. 2020).

Generally, in H II regions studies, the same temperature t_3 is used to estimate the O^{2+} and Ne^{2+} ionic abundances. This approach is based on the similarity of O^+ and Ne^+ ionization potentials, i.e. 35.12 and 40.96 eV, respectively, which indicates that both ions coexist in similar nebular regions. The same assumption is considered for O^+ and N^+, which is to assume t_2 for both cases whenever it is not possible to directly derive the T_e from the [N II]$\lambda 6584/\lambda 5755$. However, Dors et al. (2020c) found for AGNs (see also Riffel et al. 2021a) a slight deviation from the equality of the temperature for the O^+ (t_2) and N^+ [$t_e(N II)$]. Therefore, in order to test if the temperature for Ne^{2+}, defined for $t_e(Ne III)$, can be considered to be the same as t_3, we used results from the grid of AGN photoionization models built with the CLOUDY code by Carvalho et al. (2020). In Fig. 4, the model predicted values for $t_e(Ne III)$ versus t_3 are shown. In each panel of Fig. 4, the model results are discriminated in accordance with the parameters α_{ox} (botton panel), N_e (midle panel) and $\log U$ (top panel) assumed in the models. It can be seen that for $t_3 \gtrsim 1.0$, the models predict $t_e(Ne III)$ lower than t_3 and the outlier of a point can not be explained by the variation in the nebular parameter assumed in the models. It is worth mentioning that the variations in the nebular parameters produce temperatures, in most part, within the uncertainty of ± 800 K derived in direct estimates (e.g. Kennicutt et al. 2003; Hägele et al. 2008). In the top panel of Fig. 4, we can note that for objects with higher ionization parameter a high difference between the temperatures closer to the 1 to 1 relation is derived. The fit to the estimations considering all the points in Fig. 4 produces the relation

$$t_e(Ne III) = 0.1914 \times t_3^3 - 1.1344 \times t_3^2 + 2.334 \times t_3 - 0.4854. \quad (11)$$

In order to produce an additional test for ascertaining the $t_e(Ne III)$ and t_3 relations between AGNs and H II regions, we analyse the electron temperature (T_e) as well as the O^{2+}/O and Ne^{2+}/Ne ionic abundance structures along the nebular radius. In view of this, we consider photoionization models built with the CLOUDY code in order to represent both kind of objects. For both models we adopt the same nebular parameters, i.e. electron density $N_e = 500\,\text{cm}^{-3}$, solar metallicity $(Z/Z_\odot) = 1.0$, and logarithm of the ionization parameter $\log U = -2.5$. The outer radius in both AGN and H II region models was considered to be the radius at which the electron temperature of the gas reaches 4 000 K, i.e. the default lowest allowed kinetic temperature by the CLOUDY code. It is worth noting that gases cooler than $\sim 4\,000$ K practically do not emit the optical and infrared emission lines considered in this work. Despite the fact that AGNs have slightly larger N_e values (by a factor of ~ 2) than H II regions (see, e.g. Copetti et al. 2000; Vaona et al. 2012), the same value for this parameter was used in both models in order to maintain consistency. For the lower electron density regime, the N_e value does not change the temperature and ionization structure predicted by the photoionization models. For the AGN model, we adopt the SED as being a power law described by the slope $\alpha_{ox} = -1.1$ (for a detailed description of this SED see Krabbe et al. 2021). The SED
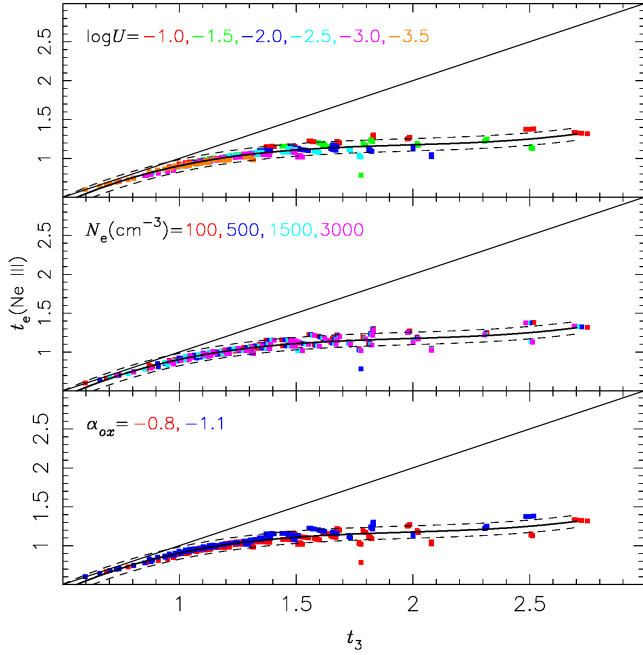
Figure 4. Temperature values for $t_e(\text{Ne\,III})$ versus t_3 predicted by the photoionization models built by Carvalho et al. (2020). Temperatures are in units of 10^4 K. The solid line represents the equality between the estimates while the continuum curve represents the fitting to the points given by Eq. 11. Dashed curves represent the deviations of Eq. 11 by ± 800 K, i.e. typical uncertainties derived in direct electron temperature estimations (e.g. Kennicutt et al. 2003; Hägele et al. 2008). In each panel, points with different colours represent photoionization models assuming different nebular parameters, as indicated.

Figure 5. Bottom panel: Profiles for the electron temperature (T_e, in units of 10^4 K) over the nebular radius predicted by AGN and H\,II region photoionization models built with the CLOUDY code (Ferland et al. 2013) versus the distance R from the innermost gas region normalized by the outermost radius R_e of each model. Different colours represent predictions for AGN and H\,II region models, as indicated. Middle and top panels: Same as bottom panel but for predictions of the fractional abundances O^{2+}/O and Ne^{2+}/Ne as indicated. The same nebular parameters are assumed in both AGN and H\,II region models: electron density $N_e = 500\,\text{cm}^{-3}$, solar metallicity ($Z/Z_\odot$) = 1.0, and logarithm of the ionization parameter $\log U = -2.5$. The AGN SED was considered as a power law described by the slope $\alpha_{ox} = -1.1$. The H\,II region SED was assumed to be a stellar cluster formed instantaneously with the age of 2.5 Myr taken from the STARBURST99 code (Leitherer et al. 1999).

for the H\,II region model was taken from STARBURST99 code (Leitherer et al. 1999) and it assumes a stellar cluster formed instantaneously with the age of 2.5 Myr, which is a typical age of normal star-forming regions (e.g. Dors et al. 2008). For detailed description of the AGN and H\,II region models see Dors et al. (2018) and Carvalho et al. (2020). The model results from AGN and H\,II region are compared with each other in Fig. 5. In the bottom panel of this figure, it can be seen that the AGN model presents a very distinct temperature distribution over the nebular radius as compared to the H\,II region one, implying that the former has a stronger decrease with the radius than the latter. Also, the O^{2+}/O and Ne^{2+}/Ne ionization structures are very distinct for both kind of objects. Similar ionic abundance distributions for both ionic ratios are derived for the H\,II region, confirming the assumption of $T_e(\text{O\,III}) \approx T_e(\text{Ne\,III})$. However, for the AGN model, the Ne^{2+}/Ne ionic abundance extends to an outer nebular radius (lower temperature) in comparison with O^{2+}/O, implying that the approach $T_e(\text{O\,III}) \approx T_e(\text{Ne\,III})$ is not valid for this object class. Moreover, the neon and oxygen ionic abundance structures for the AGN clearly indicate that the supposition $(Ne^{2+}/O^{2+}) = (\text{Ne}/\text{O})$, usually assumed to derive the total neon abundance in H\,II region studies (e.g. Kennicutt et al. 2003), can not be applied to AGNs. The result shown in Fig 4 is further supported by this simulation.
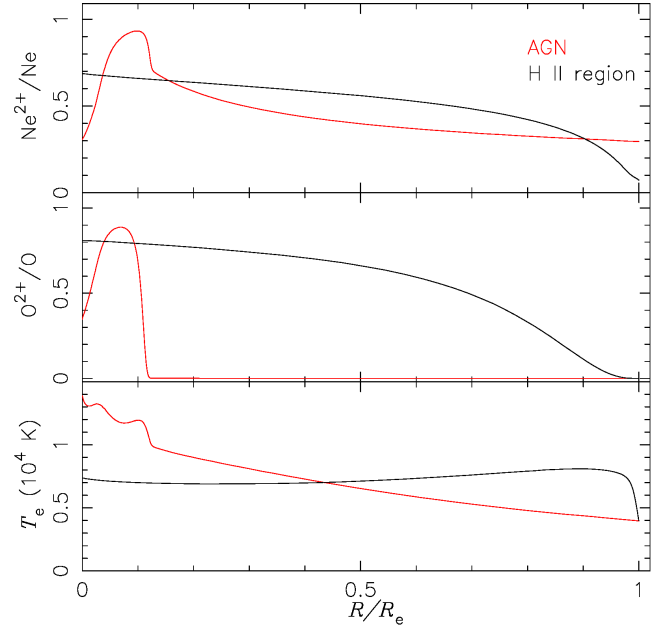
To estimate the Ne^{2+}/H^+ abundances we use the rela-

tion given by Hägele et al. (2008):

$$12 + \log\left(\frac{Ne^{2+}}{H^+}\right)_{\text{Op.}} = \log\left[\frac{I(3869\,\text{Å})}{I(H\beta)}\right] + 6.486 + \frac{1.558}{t_e}$$

$$- 0.504 \times \log t_e, \tag{12}$$

where t_e is the electron temperature. We considered both t_3 and $t_e(\text{Ne\,III})$ in the estimations for Ne^{2+}/H^+.

3.2 Infrared − lines method

The infrared−lines method (hereafter, IR-method) is based on determining the abundance of a given element using intensities of emission lines in the infrared spectral region (for a review, see Fernández-Ontiveros et al. 2017). Infrared emission lines have the advantage over optical lines for being less dependent on the electron temperature and on reddening correction, however, they have lower critical density ($10^{4-6}\,\text{cm}^{-3}$; e.g. Förster Schreiber et al. 2001) than the others ($10^{4-8}\,\text{cm}^{-3}$; e.g. Vaona et al. 2012).

Regarding the IR lines involved in our study, the

critical electron density N_c for the [Ne II]12.81μm and [Ne III]15.56μm emission lines are 7.1×10^5 and 2.1×10^5 cm^{-3} (Osterbrock & Ferland 2006), respectively. The electron densities for the NLRs of our sample (see Sect. 3.1) derived from the S$^+$ line ratio ($300 \lesssim N_e$(cm^{-3}) $\lesssim 3500$) are much lower than the N_c values. However, N_e derived from line ratios emitted by ions with different ionization potential (IP) other than the S$^+$ (IP=10.36 eV) can reveal gas regions with higher N_e values than the ones derived for our objects and, consequently, indicate an influence on physical properties based on IR lines. In fact, N_e estimates from the [O III]52μm/88μm line ratio [PI(O^{2+}) = 35.12 eV] carried out by Vermeij & van der Hulst (2002) for H II regions showed electron densities lower than $2\,000$ cm^{-3}. Also, Storchi-Bergmann et al. (2009), who built N_e map based on the [Fe II]1.533μm/1.644μm [PI(Fe$^+$) = 7.90 eV] for the NLR of NGC 4151, found values between $1\,000$ and $10\,000$ cm^{-3}. Finally, N_e determinations based on [S II]$\lambda6716/\lambda6731$ and [Ar IV$\lambda4711/\lambda4740$ [IP(A^{3+}) = 40.74 eV] line ratios in two Seyfert 2 (IC 5063 and NGC 7212) by Congiu et al. (2017) show N_e values ranging from $\sim$200 to $\sim$13 000 cm^{-3}. Although studies indicate the existence of an electron density stratification in NLRs of AGNs with values higher than the ones for our sample (see also, e.g. Kakkad et al. 2018; Freitas et al. 2018), effects of collisional de-excitation are probably negligible in our IR abundance estimates. Furthermore, we selected emissivity ratio values considering lower electron density compared to the aforementioned N_c values (see Table 1).

The Ne$^+$ and Ne^{2+} ionic abundances can be determined using the intensities of the [Ne II]12.81μm and [Ne III]15.56μm emission lines following a similar methodology presented by Dors et al. (2013). Considering two ions X^{i+} and H$^+$, the ratio of their ionic abundances is determined by

$$\frac{N(X^{i+})}{N(H^+)} = \frac{I_\lambda(X^{i+})N_e j_{\lambda(H^+)}}{I_\lambda(H^+)N_e j_{\lambda(X^{i+})}}, \qquad (13)$$

where, N(X^{i+}) and N(H$^+$) are the abundances of the X^{i+} and H$^+$ ions, I_λ(X^{i+}) is the intensity of a given emission line emitted by X^{i+}, I_λ(H$^+$) is the intensity of a reference hydrogen line, while $j_{\lambda(\text{Hi}+)}$ and $j_{\lambda(\text{X}+)}$ are the emissivity values. In Dors et al. (2013) the emissivity values were obtained from the IONIC routine of the nebular package of IRAF, which uses the Ne atomic parameters from Mendoza (1983), Saraph & Tully (1994), Galavis et al. (1997), Badnell et al. (2006), Griffin et al. (2001), Kaufman & Sugar (1986), Butler & Zeippen (1994) and McLaughlin & Bell (2000). In all abundance determinations, these emissivity values are believed to be constant as they differ by less than 5 % over a wide temperature range (Simpson 1975).

Using this method, any error in the determination of these emissivities directly translates into a systematic shift to the derived neon ionic abundance. To obtain the Ne$^+$ and Ne^{2+} ionic abundances with respect to hydrogen (H$^+$), near to mid-infrared H I recombination lines must be preferably used as reference line, such as Pα, Pβ, Pγ, Pδ, Brα, Brβ, Brγ, Brδ and Br11, which are detected in most of the sources under consideration.

The emission coefficient for lines in the infrared has a weak dependence on the electronic temperature, which, in

Table 1. H I emissivity ratio values assuming the Case B taken from Osterbrock & Ferland (2006) for electron density $N_e = 10^4$ cm^{-3} and electron temperature $T_e = 10^4$ K. k_i(Hβ), where i = 1 and 2, represent Ne$^+$/H$^+$ and Ne^{2+}/H$^+$ ionic abundance constants after the emissivity ratio values have been applied to Eqs. 14 and 15, respectively.

$j_\lambda/j_{H\beta}$	Value	$k_1(H\beta)$	$k_2(H\beta)$
		Paschen series	
$j_{P\alpha}/j_{H\beta}$	0.33200	4.389×10^{-5}	2.099×10^{-5}
$j_{P\beta}/j_{H\beta}$	0.16200	2.141×10^{-5}	1.024×10^{-5}
$j_{P\gamma}/j_{H\beta}$	0.09010	1.191×10^{-5}	5.697×10^{-6}
$j_{P\delta}/j_{H\beta}$	0.05540	7.323×10^{-6}	3.502×10^{-6}
$j_{P8}/j_{H\beta}$	0.03740	4.944×10^{-6}	2.365×10^{-6}
		Bracket series	
$j_{Br\alpha}/j_{H\beta}$	0.07780	1.028×10^{-5}	4.919×10^{-6}
$j_{Br\beta}/j_{H\beta}$	0.04470	5.909×10^{-6}	2.826×10^{-6}
$j_{Br\gamma}/j_{H\beta}$	0.02750	3.635×10^{-6}	1.738×10^{-6}
$j_{Br\delta}/j_{H\beta}$	0.01810	2.392×10^{-6}	1.144×10^{-6}
$j_{Br10}/j_{H\beta}$	0.00910	1.203×10^{-6}	5.753×10^{-7}
$j_{Br11}/j_{H\beta}$	0.00695	9.181×10^{-7}	4.391×10^{-7}
$j_{Br13}/j_{H\beta}$	0.00425	5.613×10^{-7}	2.684×10^{-7}

general, is disregarded. Therefore, abundance of a given ion can be obtained directly from the ratio between an emission line observed in the infrared and a hydrogen reference line. The calculation of Ne$^+$ and Ne^{2+} ionic abundances can be obtained by the general relations with their emission lines:

$$\frac{Ne^+}{H^+} = \frac{I(12.81\mu m)}{I(H\beta)} \times 1.322 \times 10^{-4} \qquad (14)$$

and

$$\frac{Ne^{2+}}{H^+} = \frac{I(15.56\mu m)}{I(H\beta)} \times 6.323 \times 10^{-5}, \qquad (15)$$

respectively.

Based on the above assumptions together with the values of the hydrogen line emissivities relative to Hβ listed in Table 1 and Eqs. 14 and 15, we deduce the following relations:

$$\frac{Ne^+}{H^+} = \frac{I(12.81\ \mu m)}{I(\text{Paschen})} \times k_1(H\beta), \qquad (16)$$

$$\frac{Ne^+}{H^+} = \frac{I(12.81\ \mu m)}{I(\text{Brackett})} \times k_1(H\beta), \qquad (17)$$

$$\frac{Ne^{2+}}{H^+} = \frac{I(15.56\ \mu m)}{I(\text{Paschen})} \times k_2(H\beta) \qquad (18)$$

and

$$\frac{Ne^{2+}}{H^+} = \frac{I(15.56\ \mu m)}{I(\text{Brackett})} \times k_2(H\beta), \qquad (19)$$

where $k_1(H\beta)$ and $k_2(H\beta)$ are the constants derived from the emissivity ratio values presented in Table 1.

The Case B was assumed to derive the above equations because, as opposed to the broad-line region gas, much of the narrow-line region is believed to be optically thick to the

ionizing radiation, even though studies of the He II $\lambda4686$ Å/Hβ ratio in AGNs indicates the presence of some optically thin gas (Murdin 2003). The [Ne III] $\lambda15.56$ μm line is always chosen over the [Ne III] $\lambda36.0$ μm when both are measured, because the spectrum is noisier at the long wavelength end of the long high-resolution (LH) module in the Infrared Spectrograph (IRS). Therefore, we preferred to use the [Ne III] $\lambda15.56$ μm line flux for the abundance determination of this ion, which also has larger transition probability and critical density.

4 TOTAL ABUNDANCE DETERMINATIONS

4.1 Oxygen

In general, the total abundance of an element relative to hydrogen abundance is difficult to be calculated because not all emission line intensities emitted by the ions of this element are measured in the same spectral range. This fact, in principle, is circumvent by the use of ionization correction factor (ICF) proposed by Peimbert & Costero (1969). The ICF for the unobserved ionization stages of an element X is defined as

$$\mathrm{ICF}(X^{i+}) = \frac{\mathrm{N}(X/H)}{\mathrm{N}(X^{i+}/H^+)}, \tag{20}$$

being N the abundance and X^{i+} the ion whose ionic abundance can be calculated from its observed emission lines. For instance, considering optical emission lines of oxygen, it is relatively easy to derive the O^+/H^+ and O^{2+}/H^+ abundances when T_e and N_e are derived. However, emission lines of oxygen ions with higher ionization states are observed in other spectral bands as, for instance, in X-rays (e.g. Cardaci et al. 2009; Bianchi et al. 2010; Bogdán et al. 2017). Recent studies (Flury & Moran 2020; Dors et al. 2020c) indicate that the contribution of ions with ionization stage higher than O^{2+} in AGNs is in order of 20 per cent of the total O/H abundance. A smaller contribution of these ions, at least, in poor metal star-forming regions, is in order of only 1-5 per cent (Skillman & Kennicutt 1993; Lee & Skillman 2004).

To calculate the total oxygen abundance N(O/H) for our sample, we assumed

$$\mathrm{N}\left(\frac{O}{H}\right) = \mathrm{ICF}(O) \times \mathrm{N}\left(\frac{O^{2+}}{H^+} + \frac{O^+}{H^+}\right), \tag{21}$$

where ICF(O) is the Ionization Correction Factor for oxygen. We consider the ICF(O) expression proposed by Torres-Peimbert & Peimbert (1977)

$$\mathrm{ICF}(O) = \frac{\mathrm{N}(He^+) + \mathrm{N}(He^{2+})}{\mathrm{N}(He^+)}, \tag{22}$$

(see also Izotov et al. 2006; Flury & Moran 2020). This ICF expression is based on the similarity between the He$^+$ and O^{2+} ionization potential (about 54 eV).

To calculate the ionic helium abundance for each object taking into account the assumption that $t = t_3$, we use the relations proposed by Izotov et al. (1994) expressed as,

$$\frac{\mathrm{N}(He^+)}{\mathrm{N}(H^+)} = 0.738\, t^{0.23}\, \frac{I(\lambda5876)}{I(H\beta)} \tag{23}$$

and

$$\frac{\mathrm{N}(He^{2+})}{\mathrm{N}(H^+)} = 0.084\, t^{0.14}\, \frac{I(\lambda4686)}{I(H\beta)}. \tag{24}$$

4.2 Neon

The total neon abundance determination in Seyfert 2 nuclei from either T_e or IR method can be realised by using an ICF taking into account the unobserved ionization stages ions of this element, such as Ne^{3+}, whose emission lines are observed at 12μm and 24μm (e.g. Dudik et al. 2007). Peimbert & Costero (1969) and Peimbert & Peimbert (2009), based on the similarity between the ionization structures of neon and oxygen [$(Ne^{2+}/Ne) \approx (O^{2+}/O)$], proposed

$$\mathrm{ICF}(Ne^{2+}) = \mathrm{N}\left(\frac{O}{O^{2+}}\right) \approx \mathrm{N}\left(\frac{O^+ + O^{2+}}{O^{2+}}\right). \tag{25}$$

However, this approach does not seem to be valid for AGNs. For example, Komossa & Schulz (1997), by using multi-component photoionization models which permitted a successful match of a large set of line intensities from the UV to the NIR for Seyfert 2 nuclei, showed that the Ne^{2+} ion extends to a larger (where a lower temperature is expected) radius of the AGN than O^{2+}. Similar result was found by Alexander & Balick (1997) for Planetary Nebulae (PNs), which also exhibited gas with high ionization. In fact, it can be seen from Fig. 4 that, generally, t_3 is higher than t_e(Ne III). Therefore, based on the results shown in Fig. 5, it is necessary to produce a new formalism to replace Eq. 25 for AGNs. We developed a semi-empirical neon ICF following a similar methodology assumed by Dors et al. (2013) for SFs.

The total neon abundance in relation to hydrogen is usually assumed to be

$$\frac{Ne}{H} \approx \frac{Ne^+}{H^+} + \frac{Ne^{2+}}{H^+}. \tag{26}$$

This approximation can be more reliable for SFs than AGNs, because it considers a null abundances of $Ne^{i\,>\,2+}$. We use the photoionization model results by Carvalho et al. (2020) to ascertain the validity of Eq. 26 for AGNs. In the bottom panel of Fig. 6, the model results for y = 1 − [(Ne$^+$ + Ne^{2+})/H$^+$] versus x = [$O^{2+}/(O^+ + O^{2+})$] is shown. It can be seen that, for x $\lesssim$ 0.7 or for $\log U \lesssim -2.5$ the abundance sum (Ne$^+$ + Ne^{2+}) represents more than 80 % of the total Ne abundance. In the top panel of Fig. 6, a distribution of x values for the objects in our sample, calculated by using the T_e−method (see Sect. 3.1), is shown. It can be seen that most of the objects ($\sim$90 %) have x $\lesssim$ 0.6 within the range $0.02 \leqq \mathrm{x} \leqq 0.72$. Thus, a small correction factor is necessary in Eq. 26. A fit to the points in Fig. 6 produces

$$y = (0.78 \pm 0.06)x^2 - (0.33 \pm 0.06)x + (0.07 \pm 0.01) \tag{27}$$

and Eq. 26 can be rewritten in the form

$$\frac{Ne}{H} = f \times \left(\frac{Ne^+}{H^+} + \frac{Ne^{2+}}{H^+}\right), \tag{28}$$

where

$$f = \frac{1}{1-y}. \tag{29}$$

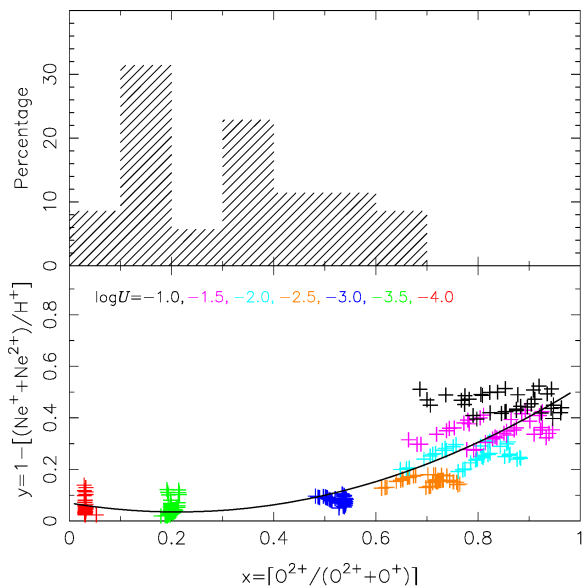**Figure 6.** Bottom panel: Neon ionic abundance ratio y = $1 - [(Ne^+ + Ne^{2+})/H^+]$ versus oxygen ionic abundance ratio x = $[O^{2+}/(O^+ + O^{2+})]$ predicted by photoionization model built by Carvalho et al. (2020). Results from photoionization models assuming distinct ionization parameter (U) values are indicated by different colours. The black solid line represents a fit to the points represented by Eq. 27. Top panel: The distribution of oxygen ionic abundance ratios for our sample of objects (see Sect. 3) calculated by using the T_e−method.

For the infrared abundance determinations, Eq. 28 was applied, where the Ne^+ and Ne^{2+} estimates were based on Eqs. 16, 17, 18 and 19 and the f factor was calculated from Eqs. 27 and 29 with x estimates obtained by using the T_e-method (see Sect. 3.1).

For Ne/H estimates based on optical lines, it is only possible to calculate the Ne^{2+}/H^+ abundance based on the Eq. 12 and assuming t_3 and $t_e(Ne\,III)$. For that, the total neon abundance estimates via optical lines must be assumed

$$\frac{Ne}{H} = ICF(Ne^{2+}) \times \frac{Ne^{2+}}{H^+}. \tag{30}$$

Using Eqs. 14, 15 and 28, we derive a semi-empirical neon ICF given by

$$ICF(Ne^{2+}) = 2.10\, f \times \left[\frac{I(12.81\ \mu m)}{I(15.56\ \mu m)} + 0.48 \right]. \tag{31}$$

The photoionization models and expressions employed to derive the ionic abundances, previously presented, probably use different set of atomic parameters which could introduce a small systematic uncertainty in the resulting abundances. However, Juan de Dios & Rodríguez (2017) found that atomic data variations introduce differences in the derived abundance ratios as low as ∼0.15 dex at low density ($N_e \lesssim 10^3$ cm^{-3}). Since most NLRs of Seyfert 2 present N_e values lower than 10^3 cm^{-3} (e.g. Vaona et al. 2012; Dors et al. 2014, 2020b; Freitas et al. 2018; Revalski et al. 2018b; Kakkad et al. 2018; Revalski et al. 2021) the consideration of distinct atomic parameters in our calculations is expected to have a small effect in our abundance results.

5 RESULTS

The bottom panel of Fig. 7 shows a comparison between the ionic abundance 12+log(Ne^{2+}/H^+) obtained using the infrared lines method (see Sect. 3.2) considering Paschen and Brackett emission lines, i.e. calculated from Eqs. 18 and 19. The average and standard deviation are derived for Ne^{2+}/H^+ estimation of each object assuming different Paschen and Brackett lines which are in order of 0.02 dex. In the top panel of Fig. 7, the mean differences between the estimations versus the estimations via Paschen lines are shown. The average difference is about 0.1 dex, similar to error derived in ionic abundance estimates by Kennicutt et al. (2003). We notice a slight trend (see Fig. 7 top panel) of Ne^{2+}/H^+ abundances via Paschen lines to be lower than those via Brackett lines, reaching up to ∼ 0.4 dex for the lowest values of Paschen neon ionic determinations. This discrepancy could suggest either some uncertainties in the physical constants of the H line ratios (probably for high temperature) or in the line measurements (e.g. aperture corrections and/or distinct calibrations in the data compiled from the literature). In any case, this result is marginal because only two objects present 12+log(Ne^{2+}/H^+) lower than ∼ 7.3 dex. If this objects are not considered, we derive about a null difference among the estimates. Thus, it is shown that the Ne^{2+}/H^+ estimates based on any IR hydrogen reference line of a particular series are in agreement with each other taken into account a discrepancy of ∼ 0.1 dex. It was possible to calculate Ne^{2+}/H^+ by using Paschen lines for 27 objects of our sample and Brackett lines for 34 objects with 26 correspondingly Paschen and Bracket emission line series.

In Table A4, the Ne^+/H^+, Ne^{2+}/H^+, f factor and the total neon abundance [12+log(Ne/H)] values for our sample obtained using IR-method (see Sect. 3.2 and 4.2) are listed. The infrared Ne^{2+}/H^+ ionic abundance values listed in Table A4 represent the mean values from the estimates based on Paschen and Brackett lines. It was not possible to calculate the Ne^+/H^+ abundance, and consequently the Ne/H, for three objects from our sample (i.e. NGC 1320, NGC 3393 and ESO428−G014) due to the absence of the [Ne II]12.81μm emission lines in the original works where the data were compiled. In Table A5, the 12+(Ne^{2+}/H^+) values calculated via T_e-method assuming t_3 and $t_e(Ne\,III)$ (see Sect. 3.1), the ICF(Ne^{2+}) obtained from Eq. 31 and the total neon abundance for our sample are listed.

In the bottom panel of Fig. 8, the Ne^{2+}/H^+ values estimated using the T_e-method, assuming $t_e(Ne\,III)$ and t_3, versus estimations obtained from IR-method are shown. In the top panel of this figure, the differences between these estimations versus the IR ionic estimates are shown. It can been seen that, for most of the objects, the IR estimations are higher than those obtained via the T_e-method by using both $t_e(Ne\,III)$ and t_3 electron temperatures. An average difference value from the comparison between the IR-method and the $t_e(Ne\,III)$ estimations is ∼ −0.20 dex. However, when t_3 is considered, an average difference between the estimates of ∼ −0.69 dex is found. The differences between the IR-method and the T_e-method estimates imply systematic differences in both cases, i.e. they increase with Ne^{2+}/H^+, until ∼ 1 dex and ∼ 2 dex, for $t_e(Ne\,III)$ and t_3, respectively. The difference between Ne^{2+}/H^+ found in Fig. 8 is due to systematic derivation (from Eq. 11) of lower

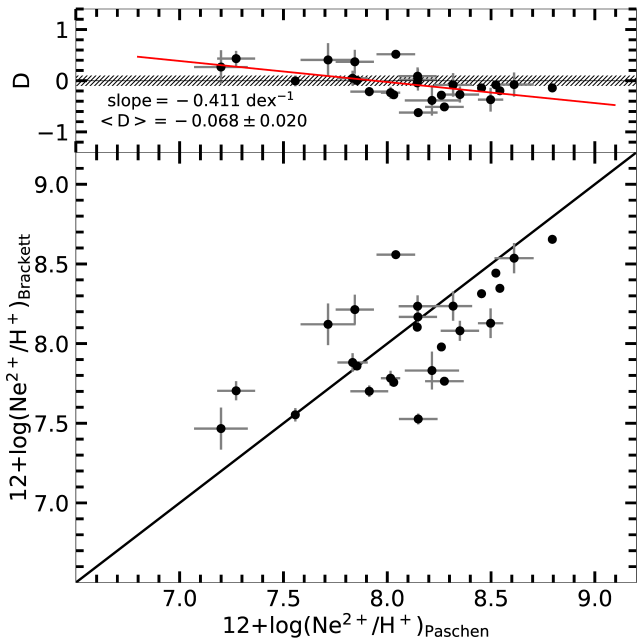**Figure 7.** Comparison between the ionic abundance of $12+\log(\mathrm{Ne^{2+}/H^+})$ derived via IR−lines by using Brackett and Paschen (see Sect. 3.2). The points represent estimations for the objects presented in Table A4. The solid line represents the equality of the two estimates. Top panel: difference (D = ordinate − abscissa) between the estimations. The black line represents the null difference, while the red line represents a linear regression to these differences whose slope is indicated. The average difference ($< D >$) is also shown. The hatched area indicates the uncertainty of ± 0.1 derived in the abundance estimations.

$t_\mathrm{e}(\mathrm{Ne\,III})$ values in comparison with t_3, which translate into higher ionic abundances when $t_\mathrm{e}(\mathrm{Ne\,III})$ is assumed. In other words, according to our photoionization model results (see Fig. 4), the [O III] temperature is likely an overestimation of the [Ne III] temperature.

Neon ICFs for AGNs are still not available in the literature, however, we can compare the values obtained for our sample with those derived for H II regions by Dors et al. (2013). These authors derived the ICF($\mathrm{Ne^{+2}}$) directly (from neon IR lines) for 23 H II regions with oxygen abundance in the range of $7.1 \lesssim 12 + \log(\mathrm{O/H}) \lesssim 8.5$ and ionization degree $0.4 \lesssim [\mathrm{O^{2+}/(O^+ + O^{2+})}] \lesssim 1.0$. Our AGN sample is based on more metallic objects $8.0 \lesssim 12 + \log(\mathrm{O/H}) \lesssim 9.2$ and similar ionization degree $0.2 \lesssim [\mathrm{O^{2+}/(O^+ + O^{2+})}] \lesssim 0.7$. From Table A5, we notice that the ICF($\mathrm{Ne^{+2}}$) values for the AGN sample range from $\sim$1.5 to $\sim$12, where the highest value (11.83) is derived for NGC 5953. Even not considering this high value, we find an ICF($\mathrm{Ne^{+2}}$) range of 1.5-6.5, a wider range of values than those derived for H II regions by Dors et al. (2013), i.e. from ~ 1 to ~ 2.

In Table A6, the $12 + (\log \mathrm{O^+/H^+})$, $12 + (\log \mathrm{O^{2+}/H^+})$, the ICF(O) (by using Eq. 31), the total oxygen abundance [$12+\log(\mathrm{O/H})$] as well as the $\log(\mathrm{Ne/O})$ values, assuming neon abundance derivations via t_3 and $t_\mathrm{e}(\mathrm{Ne\,III})$, are listed. With regard to the oxygen ICFs for the 35 objects where the values ($\sim 80\,\%$ of the sample) could be estimated, we derived values ranging from ~ 1.1 to 2.2, with an average

Table 2. Minimum, maximum and the mean abundance ratio values for our sample (see Sect. 2) derived by the use of the distinct methods (see Sects. 3 and 4). The values obtained from the abundance distributions are presented in Figs. 9 and 10.

Abundance ratio	Min.	Max.	Mean
$12+\log(\mathrm{O/H})$	8.03 ± 0.05	9.17 ± 0.06	8.55 ± 0.22
$12+\log(\mathrm{Ne/H})$-t_3	7.44 ± 0.12	8.48 ± 0.06	7.90 ± 0.24
$12+\log(\mathrm{Ne/H})$-$t_\mathrm{e}(\mathrm{Ne\,III})$	7.90 ± 0.05	8.88 ± 0.21	8.39 ± 0.22
$12+\log(\mathrm{Ne/H})$-IR	7.99 ± 0.01	9.47 ± 0.11	8.54 ± 0.36
$\log(\mathrm{Ne/O})$-t_3	-1.21 ± 0.01	$+0.03 \pm 0.03$	-0.66 ± 0.27
$\log(\mathrm{Ne/O})$-$t_\mathrm{e}(\mathrm{Ne\,III})$	-0.51 ± 0.01	$+0.58 \pm 0.03$	-0.17 ± 0.24

value of ~ 1.30, which indicates a correction in the total oxygen abundance in order of only ~ 0.1 dex (see also Flury & Moran 2020; Dors et al. 2020c).

In Fig. 9, histograms showing the distributions of total oxygen abundance (O/H) and the total neon abundances for our sample, calculated from T_e-method assuming t_3 and $t_\mathrm{e}(\mathrm{Ne\,III})$, as well as Ne/H via IR-method, are shown. The solar values $12+\log(\mathrm{O/H})_\odot = 8.69$ and $12+\log(\mathrm{Ne/H})_\odot = 8.0$, obtained by Allende Prieto et al. (2001) and Holweger (2001), respectively, are indicated in Fig. 9. In Table 2, the minimum, maximum and average values of the distributions of O/H, Ne/H and Ne/O derived using the distinct methods are listed. It can be observed that, in Fig. 9, most ($\sim 64\,\%$) of the objects for the sample have oxygen abundance in the range $8.4 \lesssim 12 + \log(\mathrm{O/H}) \lesssim 8.8$ or $0.50 \lesssim (Z/\mathrm{Z_\odot}) \lesssim 1.3$, which implies that only $8\,\%$ of oxygen abundance values are found in the low metallicity regime (i.e. $12 + \log(\mathrm{O/H}) \lesssim 8.2$). Groves et al. (2006), who considered a photoionization model sequence to reproduce the optical emission line intensities of AGNs, found a similar result, i.e. low metallicity AGNs are rarely found in the local universe. The maximum O/H value derived for our sample ($12 + \log(\mathrm{O/H}) \approx 9.2$) is about 0.2 dex higher than the maximum value derived for star-forming galaxies by Pilyugin et al. (2007), who adopted the P-method (Pilyugin 2000, 2001).

In the case of the Ne/H abundance in Fig. 9, the estimates based on t_3 indicate that most objects ($\sim 65\,\%$) present lower values than the solar value. The abundance estimates via $t_\mathrm{e}(\mathrm{Ne\,III})$ and IR-method indicate that majority ($\gtrsim 90\,\%$) of the objects have higher Ne/H abundances than the solar value. For some few objects ($\sim 10\,\%$), IR estimates indicate values rising up to 10 times the solar value.

In Fig. 10, histograms showing the Ne/O abundance ratios distribution for our sample, whose values were calculated via T_e-method by assuming t_3 and $t_\mathrm{e}(\mathrm{Ne\,III})$, are presented. No Ne/H values derived via IR-lines are considered in Fig. 10 because the O/H values are based on a distinct method, i.e. the T_e-method. The line indicating the Ne/O solar value is also depicted in this figure. We can see that the majority ($\sim 60\,\%$) of the t_3 estimates are higher than the solar ratio and all values based on $t_\mathrm{e}(\mathrm{Ne\,III})$ lead to oversolar Ne/O abundances.
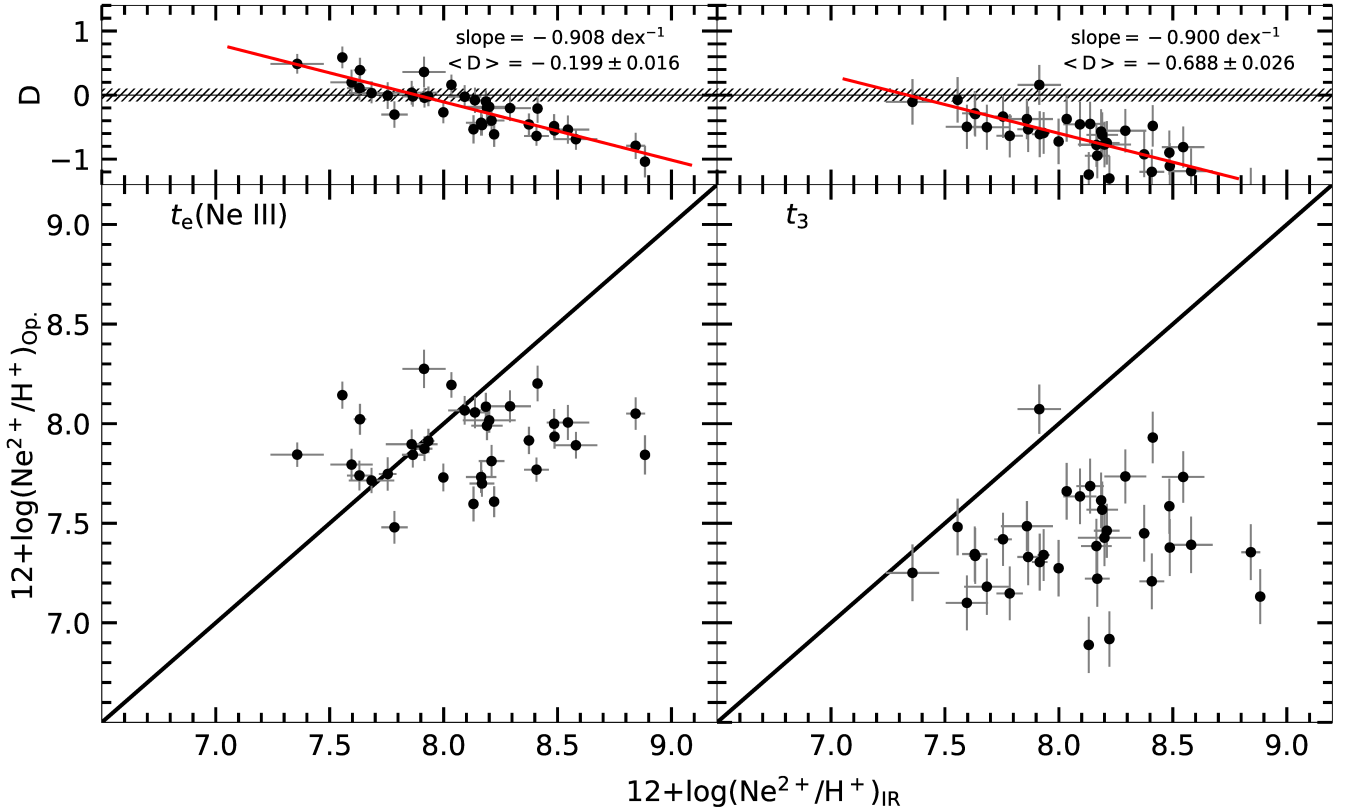
Figure 8. Same as Fig. 7 but for estimations derived using the T_e-method versus IR-method (see Sect. 3). In left panel T_e-method estimates are based on $t_e(\text{Ne III})$ and in the right panel on t_3, as indicated.
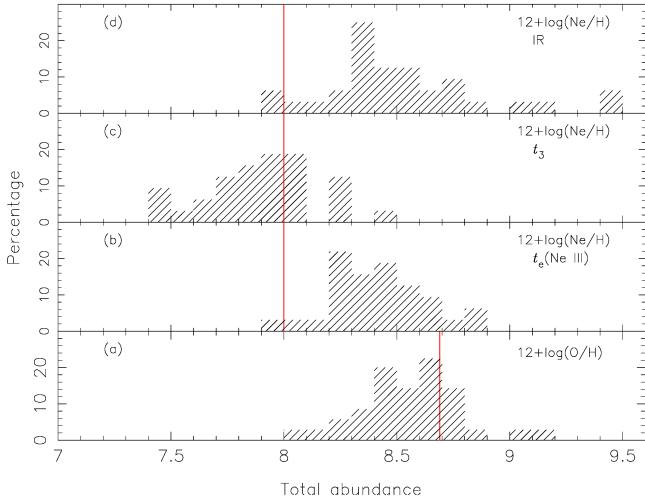

Figure 9. Histograms containing the total abundance distributions for our sample of objects (see Sect. 2). Panel (a): Distribution of $12+\log(\text{O/H})$ calculated from T_e-method (see Sects. 3.1 and 4). Panels (b) and (c): Distribution of $12+\log(\text{Ne/H})$ calculated from T_e-method assuming $t_e(\text{Ne III})$ and t_3, as indicated. (d) Distribution of $12+\log(\text{Ne/H})$ calculated from IR-method (see Sects. 3.2 and 4). Red lines indicate the $12+\log(\text{O/H})_\odot=8.69$ and the $12+\log(\text{Ne/H})_\odot=8.0$ solar values derived by Allende Prieto et al. (2001) and Holweger (2001), respectively.
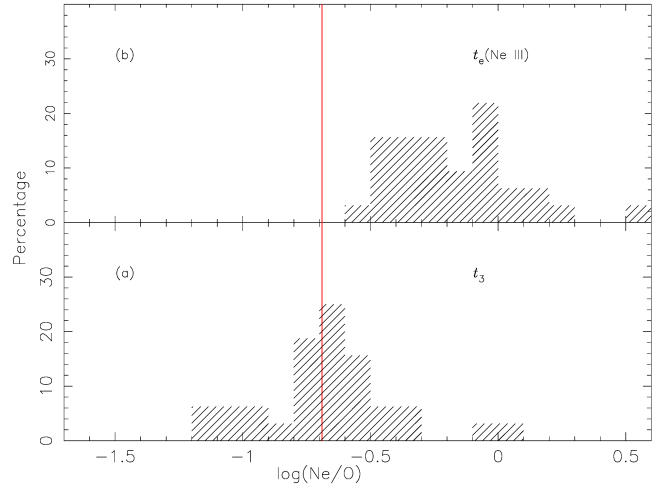

Figure 10. Same as Fig. 9 but for $\log(\text{Ne/O})$. Panels (a) and (b) show distributions obtained with Ne abundances calculated from T_e-method assuming t_3 and $t_e(\text{Ne III})$, as indicated. Red line indicates $\log(\text{Ne/O})_\odot=-0.69$ solar value (Allende Prieto et al. 2001; Holweger 2001).

6   DISCUSSION

Along decades, several studies have been carried out to address the determination of chemical abundances of AGNs at both low and high redshift, mainly based on comparing pho-

toionization model results with observational data. However, these studies have been primarily focused on the determination of the metallicity and in some few instances on the determination of oxygen and nitrogen abundances. Pertaining to the low redshift objects, where optical emission lines are easily observed, for instance, Storchi-Bergmann & Pastoriza (1990), who compared Seyfert and LINERs observational and photoionization model line predictions in the diagram [N II]($\lambda6548$ +$\lambda6584$)/Hα versus [S II]($\lambda6716$+$\lambda6731$)/Hα, found sulfur and nitrogen abundances ranging from one-half-solar to five times the solar values. After this pioneering work, Dors et al. (2017) built detailed photoionization models to reproduce narrow optical emission lines for a sample consisting of 44 local ($z < 0.1$) Seyfert 2 nuclei and found nitrogen abundances ranging from ∼0.3 to ∼ 7.5 times the solar value.

Direct elemental abundance of AGNs, based on the T_e-method, are rare in the literature. Probably, the first T_e-method estimation in AGN was undertaken by Osterbrock & Miller (1975) for Cygnus A, in the derivation of 12+log(O/H)∼ 8.60, 12+log(Ne/H)∼ 8.0 and other elemental abundances. After this pioneering work, other authors also applied the T_e-method to AGNs (e.g. Alloin et al. 1992; Izotov & Thuan 2008; Dors et al. 2015, 2020b,c) but focused mainly on O/H abundance. Recently, Flury & Moran (2020), by assuming an approach for estimating abundances of heavy elements which involves a reverse-engineering of the T_e-method, derived the first (N/O)-(O/H) relation for AGNs based on the direct method. On the other hand, for the elemental abundances in high redshift AGNs, oversolar nitrogen abundance have been derived for the most part of the objects (see Dors et al. 2019 and reference therein). In summary, hitherto, the unique neon abundance in AGNs appears to have been the derivation obtained by Osterbrock & Miller (1975), who estimated a value approximately equal to the solar abundance. In subsequent sections, we discuss the neon abundance results derived for our sample.

6.1 Ne^2/H^+ **abundance**

Vermeij & van der Hulst (2002) obtained optical (by using the Boller & Chivens spectrograph on the ESO 1.52 meter telescope) and infrared (by using Short Wavelength Spectrometer - SWS and Long Wavelength Spectrometer- LWS on board the Infrared Space Observatory - ISO) spectra for 15 H II regions located in the Magellanic Clouds. From these objects, it was possible to derive the Ne^{2+} ionic abundances via both IR and T_e−method for 13 out of the 15 H II regions. The differences (D) between these estimations ranges from −0.6 to +0.6 dex, thus, for some objects the T_e−method resulted in higher abundances. The averaged value of D was about zero. The result obtained by Vermeij & van der Hulst (2002) is in disagreement with the findings by Dors et al. (2013), who found that the abundances obtained via infrared emission lines are higher than those obtained via optical lines in H II regions, by a factor of ∼ 0.60 dex.

In Fig. 8, 12 + log(Ne^{2+}/H^+) abundances via T_e-method assuming t_e(Ne III) (left panel) and t_3 (right panel) are compared with the results via IR−method for our sample. In the top panels of Fig. 8, the differences between both estimates are plotted versus the IR estimates. As noted earlier in Fig. 8, the difference (D) is systematic in both cases,

where D increases with Ne^{2+}/H^+ from IR-method estimations. The average difference ($< D >$) between ionic abundances values via T_e-method assuming t_3 and IR estimates is obviously the same value (∼ 0.60 dex) as the average value found for H II regions by Dors et al. (2013). Therefore, probably, any artificial effects attributed to the use of heterogeneous sample of data sets, aperture effects, different regions in the objects which are considered in optical and IR observations, can have influence on our results.

The origin of D was discussed in details by Dors et al. (2013) for H II regions and it was attributed to be mainly the presence of abundance and/or electron temperature variations across the nebula rather than extinction effects in the area of the sky covered by the IR and optical observations, as proposed by Vermeij & van der Hulst (2002). An overview of the discrepancy derived from this work will be presented in a subsequent paper, even though we refer to few possible scenarios here. Recently, Dors et al. (2020a) by using the SUMA code (Viegas-Aldrovandi & Contini 1989), which assumed that the gas ionization/heating is due to photoionization and shocks, found that Seyfert 2 nuclei have gas shock velocities in the range of 50-300 km s^{-1}. These shocks can produce an extra gas heating source in the NLRs, which translates into underestimation of the elemental abundances via T_e-method in relation with abundances derived from IR lines (less dependent on temperature). As an addition support to the presence of electron temperature fluctuations in AGNs, Riffel et al. (2021a) presented 2D electron temperature maps, based on Gemini GMOS-IFU observations at spatial resolutions ranging from 110 to 280 pc, in the central region of three luminous Seyfert galaxies, where a large variation of temperatures (from ∼ 8000 to $\gtrsim 30\,000$ K) were derived. This result indicates a large fluctuation of t_3.

The Paα to Paδ and Brα to Brδ emission lines are not only the strongest emission lines found in the NIR and MIR, they are also relatively free from blending features and dust attenuation. This makes them valuable tools to derive the chemical abundances of AGNs. The optical Balmer emission lines, although stronger, can suffer blending with other lines (i.e. Hα normally blends with [N II] $\lambda6548$, $\lambda6584$ Å), and at least to some degree, are expected to be more affected by dust absorption than Paschen and Brackett emission lines. Independent measurements of the narrow component fluxes can yield important constraints on the presence of dust within the line of sight which could also affect the emitter regions of IR lines. In fact, effects of dust on hydrogen emission line measurements are clearly observable only in the Balmer emission line ratios but they can not be detected at a significant level using the Paschen and Brackett emission lines alone (Landt et al. 2008).

For the NIR broad emission line region (BLR) of AGNs, Landt et al. (2008) obtained the dust extinction in the order of $A_V \sim 1$ to ∼ 2 mag in consonance with other studies (e.g. Cohen 1983; Crenshaw et al. 2001, 2002; Storchi-Bergmann et al. 2009). From these results, the effect of the dust causing the observed extinction of the narrow emission line region depends on the location of the dust, thus, being internal dust if it is mixed with the gas phase or if it is located outside the NLR, for instance, in the host galaxy. Since the covering factor of the narrow emission line clouds is assumed to be only a few per cent, the line of sight towards the BLR will not necessarily intercept the dust. However, dust external

to the NLR will act as a screen to affect the smallest scale components such as the BLR and the continuum emitted by the accretion disk. However, reddening in Seyfert galaxies by means of NIR line ratios performed by Riffel et al. (2006), led to the fact that Sy2s tend to lie close to the locus of points of the reddening curve, with $E(B-V)$ in the interval $0.25-1.00$ mag.

Despite these drawbacks, IR transitions offer the opportunity to examine the metallicity of galaxies almost without being affected by dust extinction, therefore, it is worthwhile to be explored and used whenever possible (Moorwood et al. 1980a,b; Lester et al. 1987; Rubin et al. 1988; Tsamis et al. 2003). For instance, the metallicities of the central and obscured regions of starburst galaxies can only be accessed via far-infrared (FIR) lines, while metallicities derived via optical lines are likely related to only the outer, less dust-extincted part of these galaxies (Puglisi et al. 2017; Calabrò et al. 2018). Considering non-consensus on dust extinction in the NIR coupled with the fact that little is known about the shapes of the NIR extinction curves of the Small and Large Magellanic Cloud (for a review see, for instance, Salim & Narayanan 2020), it will probably take observations from FIR to settle IR dust extinction and its effects on metallicities in AGNs. As a result, we chose the approach to extinction correction problems to be most relevant to optical line fluxes, while we considered extinction to be essentially negligible for our infrared data.

We notice that the comparison between the ionic abundance of $12+\log(\mathrm{Ne}^{2+}/\mathrm{H}^+)$ derived via IR$-$lines by using Brackett and Paschen series presents a linear correlation with a Pearson correlation coefficient of $R = 0.70$ (see Fig. 7). Also, the twice neon ionic abundance estimations derived using the T_e-method based on $t_\mathrm{e}(\mathrm{Ne\,III})$ and t_3 have a positive linear correlation with a Pearson correlation coefficient of $R = 0.84$ (see Figs. 8 and 11). However, we find no correlation between estimations derived using the T_e- and IR-methods. Separating the Paschen and Brackett series ionic abundance estimations with or without discriminating against the outliers, we do not find any significant change in the disparity of the doubly ionized neon ionic abundance trend. Consequently, we find the use of either only Paschen or only Bracket series or both to be reliable estimations of neon ionic abundance in Seyfert 2 nuclei. Comparison of values estimated from Eqs. 7 and 11 clearly shows a high disparity between t_3 and $t_\mathrm{e}(\mathrm{Ne\,III})$. This discrepancy translate into underestimations of $12 + \log(\mathrm{Ne}^{2+}/\mathrm{H}^+)$ abundances by t_3 as compared to $t_\mathrm{e}(\mathrm{Ne\,III})$ estimates. Despite this difference and the positive correlation between the T_e-methods, there is no correlation between the T_e- and IR-methods. Therefore, it is worthwhile investigating the non-existence of mutual relation between the T_e- and IR-methods.

The temperature problem in AGNs, thus, the cause of higher electron temperature values usually derived from observational R_{O3} ratio other than predictions by photoionization models is a potential cause of the neon ionic abundance discrepancy. It is important to highlight that the origin of the electron temperature fluctuation is an open problem in nebular astrophysics. A t^2 value of ~ 0.04 typically results in an underestimation of C/H, O/H and Ne/H by about 0.2 to 0.3 dex (Peimbert 1967; Peimbert & Costero 1969). Therefore, it is extremely important to ascertain whether the fluctuations in temperature exist or whether there are

inherent potential errors from the adopted methodology. If temperature variations exist, it is imperative to better understand their nature and possibly derive some methodology to reconcile them in chemical abundance derivations. It is worth noting that, hitherto, the t^2 values available in the literature are, in most part, indirectly based on the comparison of different methods to the estimation of T_e and the majority of the studied objects are H II regions and Planetary Nebulae (PN). Only mapping the AGNs with appropriate sensitivity and spatial resolution in the temperature diagnostic lines could conceivably provide direct evidence of small or large scale fluctuations. Recently, Riffel et al. (2021b), who used the Gemini GMOS-IFU observations of three luminous nearby Seyfert galaxies (Mrk 79, Mrk 348 and Mrk 607), found electron temperature fluctuations in these objects in the same order or larger than the maximum values reported in star-forming regions and Planetary Nebulae. Thus, the discrepancy derived from optical and IR abundance estimates can be due to the presence of electron temperature fluctuations in AGNs. Moreover, another potential source of temperature fluctuations could be the presence of density variations in the gas but we did not observe high-scale of density fluctuations in our selected sample.

Furthermore, as previously stated in this paper, aperture effect is not the primary cause of the neon ionic abundance discrepancy (e.g. Dors et al. 2013, 2020b). Following from the foregoing, we point out here two potential key reasons for the absence of connection between the T_e- and IR-methods. It is worth stating from the onset that only IR tracers can explore the gas-phase elemental abundances in the interstellar medium of dusty galaxies because the IR emission lines are insensitive to interstellar reddening. Internal dust extinction could have a significant impact on the comparison of abundances obtained from IR and optical emission lines. The blue optical [Ne III]λ3869 emission line suffers more dust absorption than the IR emission lines. Secondly, unlike optical emission lines, the emissivity of IR lines has weak dependence on electron temperature, because the atomic levels involved in the transitions are much closer to the ground state as compaered to the optical.

6.2 Ne/H abundance

In this work we determine for the first time the neon abundances for a large sample of local AGNs. These abundance determinations have deep implications in the studies of the chemical evolution of galaxies and stellar nucleosynthesys, mainly because, due to their localization in the disk and according to scenario inside-out of galaxy formation (e.g. Mollá & Díaz 2005), it is expected a high metallicity in AGNs in comparison to disk H II regions.

IR spectra of AGNs have been obtained in many studies and certain properties have been extensively derived from them. For example, Genzel et al. (1998), by using ISO observations from the Infrared Astronomical Satellite (IRAS) ultraluminous galaxies, proposed a methodology to separate the relative contribution of AGNs and star-forming regions (see also Farrah et al. 2007; Weaver et al. 2010; Meléndez et al. 2014; Hood et al. 2017, among others). Also, theoretical calibrations between metallicity, ionization parameter and IR emission lines have been proposed in the literature (e.g. Nagao et al. 2011; Pereira-Santaella et al. 2017). How-
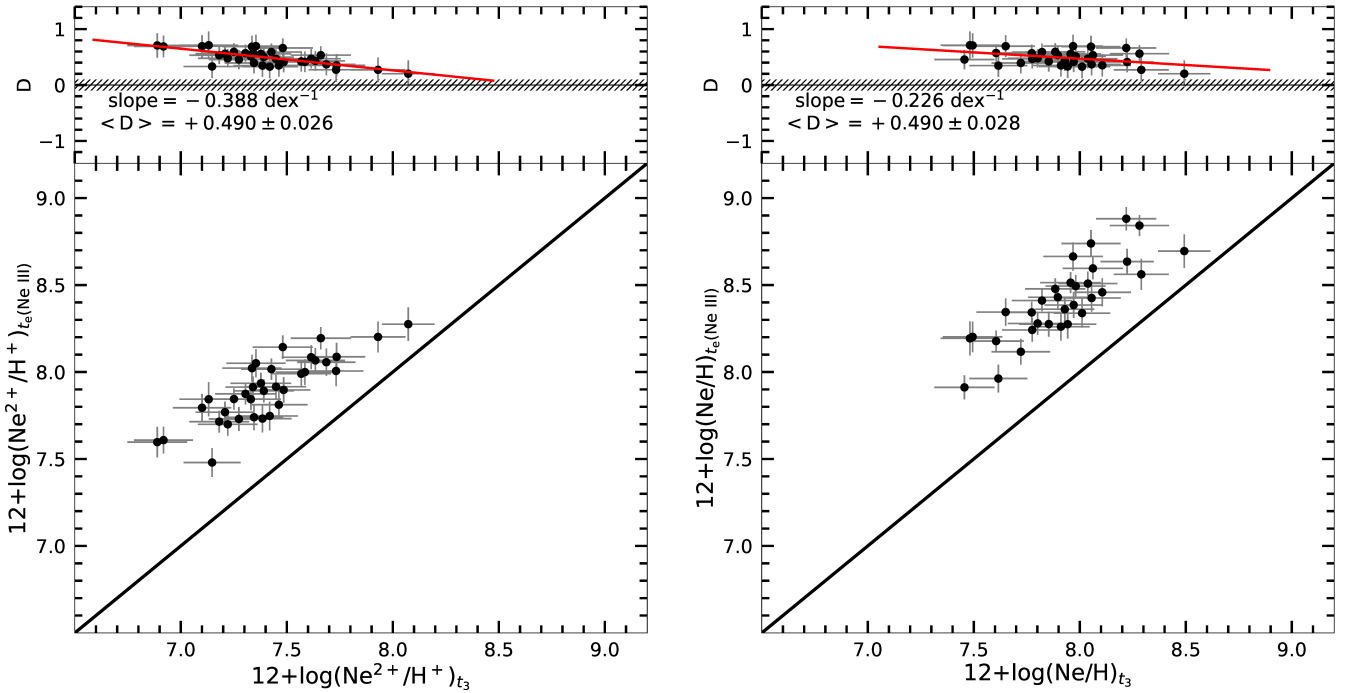
Figure 11. Same as Fig. 7 but for the ionic abundance of $12+\log(\text{Ne}^{2+}/\text{H}^+)$ and the total abundance of $12+\log(\text{Ne/H})$ derived using the T_e-methods. In both panels T_e-method estimates are based on $t_e(\text{Ne\,{\footnotesize III}})$ versus t_3, as indicated.

Table 3. Parameters of the Ne/H abundance gradients in a sample of spiral galaxies. N represents the number of H\,{\footnotesize II} regions considered in the estimations of the gradients. Y_0, $grad\,Y$ and W_0 are defined in Eqs. 32 and 33. In the last column, the original works from which the Ne/H abundance values were compiled are listed.

Galaxy	N	Y_0	$grad\,Y$	W_0	Reference
M 33	6	-4.23 ± 0.25	-0.057 ± 0.005	0.58	1
M 33	16	-4.07 ± 0.04	-0.058 ± 0.014	0.85	2
NGC 2403	6	-4.40 ± 0.03	-0.008 ± 0.005	0.40	3
NGC 3184	29	-3.57 ± 0.21	-0.080 ± 0.029	2.70	4
NGC 628	35	-4.23 ± 0.08	-0.004 ± 0.013	0.60	4
NGC 5194	8	-4.01 ± 0.20	-0.028 ± 0.037	0.97	4
NGC 5457	70	-4.05 ± 0.05	-0.021 ± 0.003	0.89	4
NGC 925	23	-3.67 ± 0.18	-0.059 ± 0.021	2.13	5
NGC 2805	8	-3.39 ± 0.19	-0.050 ± 0.015	4.07	5
NGC 4395	8	-4.13 ± 0.20	-0.056 ± 0.038	0.74	5
NGC 300	27	-4.33 ± 0.04	-0.057 ± 0.016	0.46	6

References: (1) Crockett et al. (2006), (2) Rubin et al. (2008) (3) Berg et al. (2013), (4)Berg et al. (2020), (5) van Zee et al. (1998a), (6) Bresolin et al. (2009).

ever, for the most part, these studies have not derived the elemental abundance of heavy metals (e.g. Ne, Ar, S).

Measurements of emission lines for the most abundant neon lines have been undertaken by several authors (e.g. Dasyra et al. 2011; Fernández-Ontiveros et al. 2016) but no direct determination of the neon abundance has been obtained either in AGNs or star-forming regions, mainly due to difficulty in the observation of the hydrogen reference lines and the metal lines within the same spectral range. However, using the ISO Short Wavelength Spectrometer, where recombination hydrogen and metal lines were measured, Verma et al. (2003) obtained IR data ($2.3 \lesssim \lambda(\mu\text{m}) \lesssim 45$) for 12 starburst galaxies. These authors found that Ne abundances span approximately over one up to three times order of magnitude the solar value ($1 \lesssim (\text{Ne/Ne}_\odot) \lesssim 3$). Bernard-Salas et al. (2009) obtained IR observational data (from 10 to 37 μm) for 24 starburst by using the *Spitzer* telescope and derived the Ne/H abundances ranging from ~0.60 to ~2 times the solar value. Finally, Wang & Liu (2008) obtained the neon and oxygen abundances for a large sample of Planetary Nebulae and H\,{\footnotesize II} regions, whose the observational data were compiled from the literature. Taking into account the findings of these aforementioned authors, we can assumed for SFs Ne/H values ranging from ~ 0.6 to ~ 3 times the solar value. Our Ne/H results based on T_e-method indicate a wider range of Ne/H abundances than those derived for star-forming objects, with the maximum values (see Table 2) ranging from ~ 7 to ~ 30 times the solar value when t_3 and $t_e(\text{Ne\,{\footnotesize III}})$ are considered, respectively. Similarly, we find a very high maximum value considering the Ne/H estimates based on IR lines, i.e. ~ 30 times the solar value. Thus, it appears the Ne/H abundances in AGNs reach higher values than Ne/H estimations in star-forming regions.

As an additional test, in order to verify the higher Ne/H abundance in AGNs in comparison with values derived in star-forming regions, we estimate the total neon abundance (Ne/H) in the central parts of galaxies based on the extrapolation of the radial abundance gradients of this element, which is generally found in spiral galaxies (e.g. Willner & Nelson-Patel 2002; Crockett et al. 2006; Rosolowsky & Simon 2008; Magrini et al. 2009; Stanghellini et al. 2010). This procedure helps us to infer indirect and independent values of abundances in the nuclei of spiral galaxies (e.g.

Vila-Costas & Edmunds 1992; van Zee et al. 1998b; Pilyugin et al. 2004; Zinchenko et al. 2019). As usual, we assume that the Ne/H abundance gradient is represented by

$$Y = Y_0 + grad\,Y \times R(\mathrm{kpc}), \qquad (32)$$

where $Y = \log(\mathrm{Ne/H})$, Y_0 is the extrapolated value from the Ne/H abundance to the galactic center, i.e. at radial distance $R = 0$, and $grad\,Y$ is the slope of the distribution expressed in Y units of $\mathrm{dex\,kpc^{-1}}$. As pointed out by Pilyugin et al. (2004), the reliability of radial abundance gradient determinations is defined not only by the large number of objects considered but also by the distribution of these objects along the galactic radius. Under this supposition, we take into consideration published data from the literature for Ne/H abundance values of H II regions derived by using the T_e-method and located at galactocentric distances in spiral galaxies within the range $0.2 \lesssim (R/R_{25}) \lesssim 1$, where R is the galactocentric distance and R_{25} is the B-band isophote at a surface brightness of 25 mag arcsec^{-2}. In addition, Ne/H estimations in the M 33 galaxy obtained through IR lines by Rubin et al. (2008) using *Spitzer* Space Telescope are considered. It was possible to obtain the Ne/H abundance gradients in 10 spiral galaxies. In Table 3, the identification of each galaxy, the number (N) of H II regions considered in deriving the Ne/H gradient, the Y_0 and $grad\,Y$ values as well as references to the original works from which the data were obtained are listed. Also in Table 3, the extrapolation to the central part of each galaxy of the Ne/H abundance in relation with the solar value, defined as

$$W_0 = (\mathrm{Ne/H})_0/(\mathrm{Ne/H})_\odot \qquad (33)$$

is listed. It can be seen that the extrapolated values of W_0 range from 0.40 to ~ 4.0 in Table 3, while our results indicate that AGNs have abundances of Ne/H in the range 0.30-3.00, 0.80-7.60 and 0.90-30 times the solar value, depending on the method considered (see Table 2). Also, the average value of W_0 obtained in Table 3 indicates that Ne/H abundance of ~ 1.30 times the solar value in the central parts of spiral galaxies, while our results indicate twice the average value of W_0 for AGNs (~ 2.24 times the solar value). Therefore, we certainly find that the total neon abundances from both optical and IR-lines determinations in AGNs are higher in comparison with estimations from H II regions.

6.3 Neon ICF

The total neon abundances based on IR lines combined with the ionic oxygen abundance estimates present a good opportunity to obtain an expression for the neon ICF to be applied in AGN abundance studies (Kennicutt et al. 2003; Dors et al. 2013). In most part of cases, in the optical spectra of AGN and SFs only the [Ne III]$\lambda3869$ Å line is measured, which makes the use of ICFs necessary to calculate the total neon abundance, as suggested by Peimbert & Costero (1969).

Neon ICFs for SFs have been proposed by several authors and, in most part, based on photoionization models (e.g. Izotov et al. 2006; Pérez-Montero et al. 2007; Amayo et al. 2021). Dors et al. (2013) proposed an empirical ICF for the neon based on only infrared neon lines measurements, i.e. free from the photoionization uncertainties. Unfortunately, no neon ICF expression has been proposed for AGN studies. In view of this, and following the method proposed by

Dors et al. (2013), in Fig. 12, the neon ICF values for our sample obtained from Eq. 31 versus the $O^{2+}/(O^+ + O^{2+})$ abundance ratio are shown. Inspection of ICF(Ne^{2+}) values from Table A5 reveals a very discrepant and suspicious high ICF value for NGC 5953 in comparison with other objects, therefore, it was excluded from our analysis. Despite the scattering, a clear relation between the estimates can be noted. A linear fit to the points in Fig. 12 produces

$$\mathrm{ICF(Ne^{2+})_{IR}} = -2.95(\pm1.17) \times \mathrm{x} + 4.13(\pm0.41), \qquad (34)$$

where x=[$O^{2+}/(O^+ + O^{2+})$]. This expression is valid for $0 < \mathrm{x} < 0.8$, i.e. the range of values covered by our sample of objects.

Also in Fig. 12, the ICF derived for SFs by Dors et al. (2013) given by

$$\mathrm{ICF(Ne^{2+})_{IR}} = 2.382 - 1.301\mathrm{x} + \frac{0.05}{\mathrm{x}} \qquad (35)$$

is shown. It can be noted in Fig. 12 that AGNs present higher neon ICF values than those of SFs for a fixed value of x, which is expected given their higher ionization degree.

We investigate the scattering in the points observed in Fig. 12, taking into account the dependent of the ICF(Ne^{2+})-x relation on some nebular parameters. Izotov et al. (2006) found, for some elements, a dependence between ICF-x relations and the metallicity, moreover, other authors have been investigated the ICF-x dependence with other nebular parameters (e.g. Amayo et al. 2021, 2020; Delgado-Inglada et al. 2014). In order to ascertain if the dispersion in our estimations is due to a reliance on metallicity (measured by O/H), as found by Izotov et al. (2006), the points in Fig. 12 (bottom panel) are indicated in accordance with their oxygen abundances. Also in Fig. 12 (top panel), the scattering of the ICF-x relation due to the electron density is considered. Since infrared emission-line intensities are involved in the ICF determinations and these present some dependence on the electron density, some effects from this parameter on the ICF could be derived. It can be observed from Fig. 12 that, the point positions are independent from O/H abundance and N_e values. Probably, a larger sample of objects from both infrared and optical emission lines measured with high signal-to-noise ratio, which makes it possible to derive reliable physical properties could help to improve our understanding of the source of this scattering.

6.4 Ne/O versus O/H

The primary origin of neon is derived from the stellar nucleosynthesis theory, which predicts that neon and oxygen are formed by stars of similar masses (e.g. Woosley & Weaver 1995). Thus, if stars are formed following an universal Initial Mass Function [2] (IMF, Salpeter 1955), the Ne/O abundance ratio must not be dependent on O/H abundance (or on metallicity). However, several studies on this subject have yielded conflicting results. On the one hand, Wang & Liu (2008) used direct abundance values from PN and H II regions, leading to the findings which suggested that the Ne/O ratio increases with O/H in both types of nebulae. Additionally, Guseva et al. (2011) also used a large sample of SFs and

---

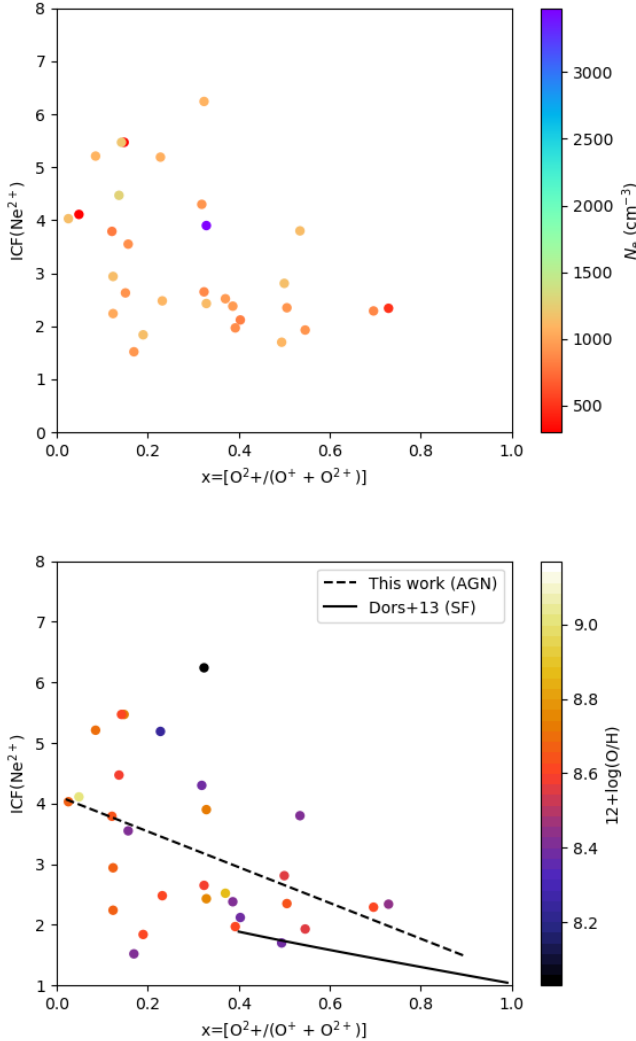[2] For a discussion on the universality of the IMF see, for example, Bastian et al. (2010).

Figure 12. Relation between ICF(Ne^{2+}) and and x=[$O^{2+}/(O^+ + O^{2+})$] ionic abundance ratio. Points represent direct estimates for our sample (see Sect. 2) whose ICF(Ne^{2+}) and x are calculated by using Eq. 31 and the T_e-method (see Sect. 3.1). Bottom panel: Red line represents a fitting to the points obtained by using Eq. 34. Black line represent the relation for SFs derived by Dors et al. (2013) assuming the same methodology and given by Eq. 35. Colour bars indicate the 12+log(O/H) value for each object. Top panel. As bottom panel but the colour bars indicate the electron density (N_e) for each object calculated through the [S II]$\lambda6716/\lambda6731$ (see Sect.3.1).

found a slight increase in Ne/O with O/H, which was interpreted by these authors as if this small increment would be likely due to a stronger depletion of oxygen onto dust grains in higher metallicity objects. On the other hand, several authors have derived a constant relation between Ne/O and O/H based on independent sample of data and ICFs (e.g. Kennicutt et al. 2003; Dors et al. 2013; Croxall et al. 2016; Arellano-Córdova et al. 2020).

In the advent of the CHemical Abundances of Spirals (CHAOS) project, thousands of direct abundances for the

heavy elements have been possible in H II regions located in spiral disks (Berg et al. 2015; Croxall et al. 2015, 2016; Berg et al. 2020; Skillman et al. 2020). These H II regions present a wide range of metallicities [$7.8 \lesssim 12 + \log(O/H) \lesssim 9.0$ or $0.10 \lesssim (Z/Z_\odot) \lesssim 2$] and play an important role in the chemical abundance studies. This homogeneous sample combined with star-forming data from the literature and our abundance results expand direct abundance determination in the emitting line objects at $(Z/Z_\odot) \gtrsim 3$, providing a unique opportunity to analyse the neon nucleosynthesis in the widest range of metallicity than previous studies. In Fig. 13, we show the Ne/O versus O/H results for our AGN sample, considering neon estimations based on T_e- method assuming t_3 (left panel) and $t_e(Ne\,III)$ (right panel). Estimates from the CHAOS project and abundance results of star-forming regions (H II regions and H II galaxies) taken from the literature, as well as polynomial fits to these estimations, are also shown in Fig. 13. Considering all the estimates (SFs and AGNs) we found

$$\log(Ne/O)_{t_3} = a_1 x^4 + b_1 x^3 + c_1 x^2 + d_1 x + e_1 \qquad (36)$$

and

$$\log(Ne/O)_{t_e(Ne\,III)} = a_2 x^4 + b_2 x^3 + c_2 x^2 + d_2 x + e_2 \qquad (37)$$

where $a_1 = 0.153$, $b_1 = -4.825$, $c_1 = 5.689 \times 10^{+1}$, $d_1 = -2.975 \times 10^{+2}$, $e_1 = 5.816 \times 10^{+2}$, $a_2 = 1.084 \times 10^{-1}$, $b_2 = -3.279$, $c_2 = 3.713 \times 10^{+1}$, $d_2 = -1.865 \times 10^{+2}$, $e_2 = 3.500 \times 10^{+2}$ and $x = 12 + \log(O/H)$.

In Fig. 13, we observe a better agreement between SF estimates and those for AGNs when t_3 is assumed (left panel) instead of $t_e(Ne\,III)$ (rigth panel). For the very high metallicity regime [$12 + \log(O/H) \gtrsim 8.80$ or $(Z/Z_\odot) \gtrsim 1.3$] an oversolar Ne/O abundance is derived, which is more conspicuous in the estimations via $t_e(Ne\,III)$. Dors et al. (2020c), by using photoionization model results, found that theoretical relations between temperatures derived for AGNs differ considerably from those for H II regions. This is due to the fact that AGNs present a very different ionization structure caused by, for instance, gas outflows (e.g. Riffel et al. 2018) and gas shocks in the ionized-neutral region transition (Dors et al. 2020a). In fact, recently, Riffel et al. (2021a) obtained from Gemini Multi-Object Spectrograph-integral field unit observations at spatial resolutions of 110–280 pc of three luminous Seyfert galaxies: Mrk 79, Mrk 348, and Mrk 607. These authors found shocks due to gas outflows play an important role in the observed temperature distributions, which can produce very different electron temperature distribution than those in H II regions (see, for instance, Riffel et al. 2021b). Based on these results, we suggest that $T_e(Ne\,III)$ must be used in the derivation of Ne^{2+} ionic abundance, instead of t_3.

The observed increase in Ne/O can be attributed to two factors. First, it can be explained by the fact that higher dust depletion of oxygen occurs in the NLRs than in SFs. Some fraction of the oxygen, in order of 0.1-0.2 dex, is expected to be trapped in dust grains in SFs (Esteban et al. 1998) and in the Interstellar Medium (ISM) along the Galactic disk (Cartledge et al. 2006; Jenkins 2009). While AGNs may have a higher rate of oxygen depletion onto dust in molecular clouds, it is unlikely that their abundance values vary significantly from SFs abundance estimations (e.g. Sternberg

et al. 1994). Moreover, Ferguson et al. (1997) and Nagao et al. (2003) concluded that refractory elements are not depleted in the coronal line region of NLRs, indicating a low dust abundance in AGNs, probably due to the destruction of grains by the hard radiation from the supermassive black hole accretion disk. Therefore, in principle, we can exclude the oxygen depletion as the origin for high Ne/O values in AGNs.

In Fig. 13, we also notice that a value of 0.5 dex oxygen depletion in NLRs is necessary to conciliate the high Ne/O abundance values with those derived for the majority of the objects. However, such level of depletion is not observed in SFs and in the ISM. Additionally, the Ne/O increase with O/H is noted in both AGNs and SFs. Furthermore, the Ne/O deviation from applying $t_e(\text{Ne\,III})$ is not due to the ICF, because the ICF was applied to both t_3 and $t_e(\text{Ne\,III})$ estimates, and the Ne/O from t_3 still agrees with SFs estimations. The total neon abundance estimations derived using the T_e-method based on $t_e(\text{Ne\,III})$ and t_3 have a positive linear correlation with a Pearson correlation coefficient of $R = 0.83$ (see Fig. 11). Therefore, it is unlikely that the offset in Fig. 13 is due to oxygen depletion. Another plausible explanation for the Ne/O increase with O/H at high metallicity is that neon, in a similar way as nitrogen and carbon, may have a secondary origin in stellar nucleosynthesis, but at an oversolar metallicity. The stellar nucleosynthesis studies by Woosley & Weaver (1995) and even more recent studies (e.g. Iwamoto et al. 1999; Kobayashi et al. 2006, 2011; Ritter et al. 2018) did not investigate star formation in environments with metallicities higher than the solar value, despite the fact that Z appears to have an impact on the stellar product (e.g. Gronow et al. 2021).

7 CONCLUSIONS

We compiled infrared and optical emission line fluxes from the literature for 35 Seyfert 2 galaxies in the local universe $(0 \lesssim z \lesssim 0.06)$ and these emission lines were used to derive the ionic $\text{Ne}^{2+}/\text{H}^+$ and elemental Ne/H abundances through the T_e-method and the IR-method. Also, O/H abundances were derived by using the T_e-method for our sample. We obtained the following conclusions:

(i) We derived $\text{Ne}^{2+}/\text{H}^+$ ionic abundances using optical and IR emission lines. We found that the ionic abundance ratio derived via IR emission lines are higher than those calculated from optical lines by the factors of 0.69 ± 0.03 dex and 0.20 ± 0.02 dex when t_3 and $t_e(\text{Ne\,III})$ are assumed in the determinations relying on the T_e-method, respectively.

(ii) The $\text{Ne}^{2+}/\text{H}^+$ abundance differences derived from the comparison between the T_e−method (assuming t_3 to derive $\text{Ne}^{2+}/\text{H}^+$) and the IR−method estimations are similar to those derived in nearby H II regions.

(iii) We found no correlation between estimations derived using the T_e− and IR−methods.

(iv) We have demonstrated from photoionization model results that, the assumption $T_e(\text{O\,III}) \approx T_e(\text{Ne\,III})$ which is valid in H II regions, is not applicable to AGNs. As a result, we proposed a new relation between electron temperature $T_e(\text{Ne\,III})$ and $T_e(\text{O\,III})$, i.e. the temperatures in the gas phase where the Ne^{2+} and O^{2+} are located, respectively.

(v) We proposed a semi-empirical Ionization Correction Factor (ICF) for neon based on [Ne II]$12.81\mu m$, [Ne III]$15.56\mu m$ which is derived from oxygen ionic abundance ratio x=[$\text{O}^{2+}/(\text{O}^+ + \text{O}^{2+})$]. The scattering in the ICF(Ne^2)-x relation does not correlate with the O/H abundance as well as the electron density.

(vi) We found that the average Ne/H value in AGNs is a factor of 2 times higher than estimations for star-forming regions (SFs). The maximum Ne/H abundance derived for our sample spans from 8 to 30 times the solar value, a factor of $\sim$ 4-10 times the maximum Ne/H value derived in SFs.

(vii) An increase in Ne/O with O/H was observed for the very high metallicity regime $[12 + \log(\text{O/H}) \gtrsim 8.80]$ when estimates for SFs are combined with the ones for AGNs. We suggest that this phenomenon is due to secondary stellar production of the neon at very high metallicity regime rather than oxygen depletion onto dust.

8 DATA AVAILABILITY

The data underlying this article will be shared on reasonable request with the corresponding author.

REFERENCES

Agostino C. J., et al., 2021, arXiv e-prints, p. arXiv:2108.07812
Alexander J., Balick B., 1997, AJ, 114, 713
Allende Prieto C., Lambert D. L., Asplund M., 2001, ApJ, 556, L63
Alloin D., Bica E., Bonatto C., Prugniel P., 1992, A&A, 266, 117
Álvarez-Álvarez M., Díaz A. I., Terlevich E., Terlevich R., 2015, MNRAS, 451, 3173
Amayo A., Delgado-Inglada G., García-Rojas J., 2020, MNRAS, 492, 950
Amayo A., Delgado-Inglada G., Stasińska G., 2021, MNRAS, 505, 2361
Arellano-Córdova K. Z., Rodríguez M., 2020, MNRAS, 497, 672
Arellano-Córdova K. Z., Esteban C., García-Rojas J., Méndez-Delgado J. E., 2020, MNRAS, 496, 1051
Badnell N. R., et al., 2006, in Barlow M. J., Méndez R. H., eds, IAU Symposium Vol. 234, Planetary Nebulae in our Galaxy and Beyond. pp 211–218, doi:10.1017/S1743921306002997
Baldwin J. A., Phillips M. M., Terlevich R., 1981, PASP, 93, 5
Bastian N., Covey K. R., Meyer M. R., 2010, ARA&A, 48, 339
Bennert N., Jungwiert B., Komossa S., Haas M., Chini R., 2006, A&A, 446, 919

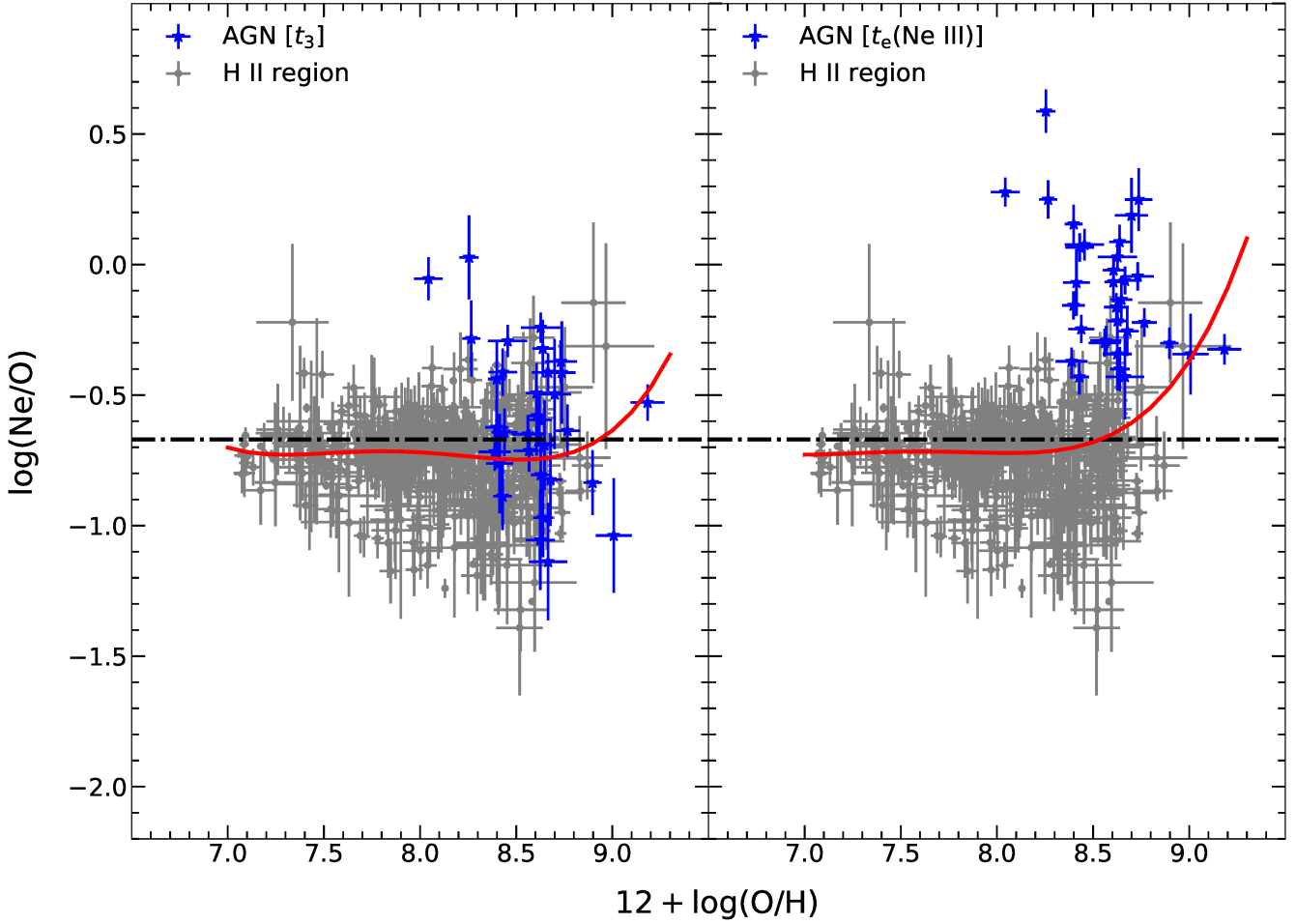**Figure 13.** Relation between log(Ne/O) and 12+log(O/H). Blue points represent estimations for our sample of Seyfert 2 obtained by using T_e-method where Ne abundances are calculated assuming t_3 (left panel) and t_e(Ne III) (right panel). Grey points represent estimations obtained by using T_e-method for star-forming regions (H II regions and H II galaxies) taken from CHAOS project (Berg et al. 2015; Croxall et al. 2015, 2016; Berg et al. 2020; Skillman et al. 2020), Hägele et al. (2006, 2008) and Pérez-Montero et al. (2007) . The red solid lines represent the polynomial fits to the points (Eqs. 36 and 37, respectively). Dashed black line represents log(Ne/O) = −0.67 (Nieva & Przybilla 2012).

Berg D. A., Skillman E. D., Garnett D. R., Croxall K. V., Marble A. R., Smith J. D., Gordon K., Kennicutt Robert C. J., 2013, ApJ, 775, 128

Berg D. A., Skillman E. D., Croxall K. V., Pogge R. W., Moustakas J., Johnson-Groh M., 2015, ApJ, 806, 16

Berg D. A., Pogge R. W., Skillman E. D., Croxall K. V., Moustakas J., Rogers N. S. J., Sun J., 2020, ApJ, 893, 96

Bergvall N., Johansson L., Olofsson K., 1986, A&A, 166, 92

Bernard-Salas J., et al., 2009, ApJS, 184, 230

Bianchi S., Chiaberge M., Evans D. A., Guainazzi M., Baldi R. D., Matt G., Piconcelli E., 2010, MNRAS, 405, 553

Boer B., Schulz H., 1993, A&A, 277, 397

Bogdán Á., Kraft R. P., Evans D. A., Andrade-Santos F., Forman W. R., 2017, ApJ, 848, 61

Böker T., Falcón-Barroso J., Schinnerer E., Knapen J. H., Ryder S., 2008, AJ, 135, 479

Bresolin F., Gieren W., Kudritzki R.-P., Pietrzyński G., Urbaneja M. A., Carraro G., 2009, ApJ, 700, 309

Brinchmann J., Charlot S., Kauffmann G., Heckman T., White S. D. M., Tremonti C., 2013, MNRAS, 432, 2112

Bryant J. J., Hunstead R. W., 1999, MNRAS, 308, 431

Butler K., Zeippen C. J., 1994, A&AS, 108, 1

Calabrò A., et al., 2018, ApJ, 862, L22

Cardaci M. V., Santos-Lleó M., Krongold Y., Hägele G. F., Díaz A. I., Rodríguez-Pascual P., 2009, A&A, 505, 541

Cardelli J. A., Clayton G. C., Mathis J. S., 1989, ApJ, 345, 245

Cartledge S. I. B., Lauroesch J. T., Meyer D. M., Sofia U. J., 2006, ApJ, 641, 327

Carvalho S. P., et al., 2020, MNRAS, 492, 5675

Castro C. S., Dors O. L., Cardaci M. V., Hägele G. F., 2017, MNRAS, 467, 1507

Cohen R. D., 1983, ApJ, 273, 489

Congiu E., et al., 2017, MNRAS, 471, 562

Contini M., 2017, MNRAS, 469, 3125

Cooke A. J., Baldwin J. A., Ferland G. J., Netzer H., Wilson A. S., 2000, ApJS, 129, 517

Copetti M. V. F., Mallmann J. A. H., Schmidt A. A., Castañeda H. O., 2000, A&A, 357, 621

Crenshaw D. M., Kraemer S. B., Bruhweiler F. C., Ruiz J. R., 2001, ApJ, 555, 633

Crenshaw D. M., et al., 2002, ApJ, 566, 187

Crockett N. R., Garnett D. R., Massey P., Jacoby G., 2006, ApJ,

637, 741

Croxall K. V., Pogge R. W., Berg D. A., Skillman E. D., Moustakas J., 2015, ApJ, 808, 42

Croxall K. V., Pogge R. W., Berg D. A., Skillman E. D., Moustakas J., 2016, ApJ, 830, 4

Curti M., Cresci G., Mannucci F., Marconi A., Maiolino R., Esposito S., 2017, MNRAS, 465, 1384

D'Agostino J. J., Poetrodjojo H., Ho I. T., Groves B., Kewley L., Madore B. F., Rich J., Seibert M., 2018, MNRAS, 479, 4907

D'Agostino J. J., et al., 2019, MNRAS, 487, 4153

Dametto N. Z., et al., 2019, MNRAS, 482, 4437

Dasyra K. M., Ho L. C., Netzer H., Combes F., Trakhtenbrot B., Sturm E., Armus L., Elbaz D., 2011, ApJ, 740, 94

Davies R. L., Rich J. A., Kewley L. J., Dopita M. A., 2014a, MNRAS, 439, 3835

Davies R. L., Kewley L. J., Ho I. T., Dopita M. A., 2014b, MNRAS, 444, 3961

Davies R., et al., 2020, MNRAS, 498, 4150

De Robertis M. M., Osterbrock D. E., 1986, ApJ, 301, 98

De Robertis M. M., Dufour R. J., Hunt R. W., 1987, J. R. Astron. Soc. Canada, 81, 195

Delgado-Inglada G., Morisset C., Stasińska G., 2014, MNRAS, 440, 536

Deo R. P., Crenshaw D. M., Kraemer S. B., Dietrich M., Elitzur M., Teplitz H., Turner T. J., 2007, ApJ, 671, 124

Díaz Á. I., Terlevich E., Castellanos M., Hägele G. F., 2007, MNRAS, 382, 251

Dopita M. A., et al., 2015, ApJS, 217, 12

Dors O. L., 2021, MNRAS, 507, 466

Dors O. L. J., Storchi-Bergmann T., Riffel R. A., Schimdt A. A., 2008, A&A, 482, 59

Dors O. L., et al., 2013, MNRAS, 432, 2512

Dors O. L., Cardaci M. V., Hägele G. F., Krabbe Â. C., 2014, MNRAS, 443, 1291

Dors O. L., Cardaci M. V., Hägele G. F., Rodrigues I., Grebel E. K., Pilyugin L. S., Freitas-Lemes P., Krabbe A. C., 2015, MNRAS, 453, 4102

Dors O. L. J., Arellano-Córdova K. Z., Cardaci M. V., Hägele G. F., 2017, MNRAS, 468, L113

Dors O. L., Agarwal B., Hägele G. F., Cardaci M. V., Rydberg C.-E., Riffel R. A., Oliveira A. S., Krabbe A. C., 2018, MNRAS, 479, 2294

Dors O. L., Monteiro A. F., Cardaci M. V., Hägele G. F., Krabbe A. C., 2019, MNRAS, 486, 5853

Dors O. L., Contini M., Riffel R. A., Pérez-Montero E., Krabbe A. C., Cardaci M. V., Hägele G. F., 2020a, MNRAS,

Dors O. L., et al., 2020b, MNRAS, 492, 468

Dors O. L., Maiolino R., Cardaci M. V., Hägele G. F., Krabbe A. C., Pérez-Montero E., Armah M., 2020c, MNRAS, 496, 3209

Dudik R. P., Weingartner J. C., Satyapal S., Fischer J., Dudley C. C., O'Halloran B., 2007, ApJ, 664, 71

Durret F., 1994, A&AS, 105, 57

Elmegreen D. M., Chromey F. R., McGrath E. J., Ostenson J. M., 2002, AJ, 123, 1381

Esteban C., Peimbert M., Torres-Peimbert S., Escalante V., 1998, MNRAS, 295, 401

Farrah D., et al., 2007, ApJ, 667, 149

Feltre A., Charlot S., Gutkin J., 2016, MNRAS, 456, 3354

Ferguson J. W., Korista K. T., Ferland G. J., 1997, ApJS, 110, 287

Ferland G. J., Netzer H., 1983, ApJ, 264, 105

Ferland G. J., Osterbrock D. E., 1986, ApJ, 300, 658

Ferland G. J., Truran J. W., 1980, ApJ, 240, 608

Ferland G. J., et al., 2013, Rev. Mex. Astron. Astrofis., 49, 137

Fernández-Ontiveros J. A., Spinoglio L., Pereira-Santaella M., Malkan M. A., Andreani P., Dasyra K. M., 2016, ApJS, 226, 19

Fernández-Ontiveros J. A., et al., 2017, Publ. Astron. Soc. Australia, 34, e053

Ferruit P., Wilson A. S., Whittle M., Simpson C., Mulchaey J. S., Ferland G. J., 1999, ApJ, 523, 147

Finkelman I., et al., 2008, MNRAS, 390, 969

Fitzpatrick E. L., 1999, PASP, 111, 63

Flury S. R., Moran E. C., 2020, MNRAS, 496, 2191

Förster Schreiber N. M., Genzel R., Lutz D., Kunze D., Sternberg A., 2001, ApJ, 552, 544

Freitas I. C., et al., 2018, MNRAS, 476, 2760

Galavis M. E., Mendoza C., Zeippen C. J., 1997, A&AS, 123, 159

Garnett D. R., Dufour R. J., Peimbert M., Torres-Peimbert S., Shields G. A., Skillman E. D., Terlevich E., Terlevich R. J., 1995, ApJ, 449, L77

Gaskell C. M., 1982, PASP, 94, 891

Gaskell C. M., 1984, Astrophys. Lett., 24, 43

Gaskell C. M., Ferland G. J., 1984, PASP, 96, 393

Genzel R., et al., 1998, ApJ, 498, 579

Gilli R., Maiolino R., Marconi A., Risaliti G., Dadina M., Weaver K. A., Colbert E. J. M., 2000, A&A, 355, 485

Goldader J. D., Joseph R. D., Doyon R., Sand ers D. B., 1995, ApJ, 444, 97

Goldader J. D., Joseph R. D., Doyon R., Sand ers D. B., 1997, ApJS, 108, 449

Gonzalez Delgado R. M., Perez E., 1996, MNRAS, 281, 781

Goodrich R. W., Osterbrock D. E., 1983, ApJ, 269, 416

Goulding A. D., Alexander D. M., 2009, MNRAS, 398, 1165

Griffin D. C., Mitnik D. M., Badnell N. R., 2001, Journal of Physics B Atomic Molecular Physics, 34, 4401

Gronow S., Cote B., Lach F., Seitenzahl I. R., Collins C. E., Sim S. A., Roepke F. K., 2021, arXiv e-prints, p. arXiv:2103.14050

Groves B. A., Heckman T. M., Kauffmann G., 2006, MNRAS, 371, 1559

Guo Y., et al., 2020, ApJ, 898, 26

Guseva N. G., Izotov Y. I., Stasińska G., Fricke K. J., Henkel C., Papaderos P., 2011, A&A, 529, A149

Hägele G. F., Pérez-Montero E., Díaz Á. I., Terlevich E., Terlevich R., 2006, MNRAS, 372, 293

Hägele G. F., Díaz Á. I., Terlevich E., Terlevich R., Pérez-Montero E., Cardaci M. V., 2008, MNRAS, 383, 209

Hägele G. F., Díaz Á. I., Terlevich R., Terlevich E., Bosch G. L., Cardaci M. V., 2013, MNRAS, 432, 810

Halpern J. P., 1982, PhD thesis, Harvard University, Cambridge, MA.

Halpern J. P., Steiner J. E., 1983, ApJ, 269, L37

Hamann F., Ferland G., 1993, ApJ, 418, 11

Heckman T. M., 1980, A&A, 500, 187

Henry R. B. C., 1993, MNRAS, 261, 306

Ho L. C., Filippenko A. V., Sargent W. L. W., 1993, ApJ, 417, 63

Holweger H., 2001, in Wimmer-Schweingruber R. F., ed., American Institute of Physics Conference Series Vol. 598, Joint SOHO/ACE workshop "Solar and Galactic Composition". pp 23–30 (arXiv:astro-ph/0107426), doi:10.1063/1.1433974

Hood C. E., Barth A. J., Ho L. C., Greene J. E., 2017, ApJ, 838, 26

Hummer D. G., Storey P. J., 1987, MNRAS, 224, 801

Imanishi M., Nakagawa T., Shirahata M., Ohyama Y., Onaka T., 2010, ApJ, 721, 1233

Iwamoto K., Brachwitz F., Nomoto K., Kishimoto N., Umeda H., Hix W. R., Thielemann F.-K., 1999, ApJS, 125, 439

Izotov Y. I., Thuan T. X., 2008, ApJ, 687, 133

Izotov Y. I., Thuan T. X., Lipovetsky V. A., 1994, ApJ, 435, 647

Izotov Y. I., Stasińska G., Meynet G., Guseva N. G., Thuan T. X., 2006, A&A, 448, 955

Jenkins E. B., 1987, Element Abundances in the Interstellar Atomic Material. Springer, p. 533, doi:10.1007/978-94-009-3861-8_20

Jenkins E. B., 2009, ApJ, 700, 1299
Ji X., Yan R., 2020, MNRAS,
Juan de Dios L., Rodríguez M., 2017, MNRAS, 469, 1036
Kakkad D., et al., 2018, A&A, 618, A6
Kaler J. B., 1976, ApJS, 31, 517
Kauffmann G., et al., 2003, MNRAS, 341, 33
Kaufman V., Sugar J., 1986, Journal of Physical and Chemical Reference Data, 15, 321
Kawara K., Nishida M., Phillips M. M., 1989, ApJ, 337, 230
Kennicutt Robert C. J., Bresolin F., Garnett D. R., 2003, ApJ, 591, 801
Kewley L. J., Dopita M. A., Sutherland R. S., Heisler C. A., Trevena J., 2001, ApJ, 556, 121
Kewley L. J., Jansen R. A., Geller M. J., 2005, PASP, 117, 227
Kewley L. J., Maier C., Yabe K., Ohta K., Akiyama M., Dopita M. A., Yuan T., 2013, ApJ, 774, L10
Kewley L. J., Nicholls D. C., Sutherland R. S., 2019, Annual Review of Astronomy and Astrophysics, 57, 511
Kobayashi C., Umeda H., Nomoto K., Tominaga N., Ohkubo T., 2006, ApJ, 653, 1145
Kobayashi C., Karakas A. I., Umeda H., 2011, MNRAS, 414, 3231
Komossa S., Schulz H., 1997, A&A, 323, 31
Koski A. T., 1978, ApJ, 223, 56
Krabbe A. C., Oliveira C. B., Zinchenko I. A., Hernández-Jiménez J. A., Dors O. L., Hägele G. F., Cardaci M. V., Telles N. R., 2021, MNRAS, 505, 2087
Kraemer S. B., Wu C.-C., Crenshaw D. M., Harrington J. P., 1994, ApJ, 435, 171
Landt H., Bentz M. C., Ward M. J., Elvis M., Peterson B. M., Korista K. T., Karovska M., 2008, ApJS, 174, 282
Lee H., Skillman E. D., 2004, ApJ, 614, 698
Leitherer C., et al., 1999, ApJS, 123, 3
Lester D. F., Dinerstein H. L., Werner M. W., Watson D. M., Genzel R., Storey J. W. V., 1987, ApJ, 320, 573
Lutz D., Maiolino R., Moorwood A. F. M., Netzer H., Wagner S. J., Sturm E., Genzel R., 2002, A&A, 396, 439
Magrini L., Stanghellini L., Villaver E., 2009, ApJ, 696, 729
Malkan M. A., Jensen L. D., Rodriguez D. R., Spinoglio L., Rush B., 2017, ApJ, 846, 102
Matsuoka K., Nagao T., Maiolino R., Marconi A., Taniguchi Y., 2009, A&A, 503, 721
Matsuoka K., Nagao T., Marconi A., Maiolino R., Mannucci F., Cresci G., Terao K., Ikeda H., 2018, A&A, 616, L4
McCall M. L., 2004, AJ, 128, 2144
McLaughlin B. M., Bell K. L., 2000, Journal of Physics B Atomic Molecular Physics, 33, 597
Meléndez M., Heckman T. M., Martínez-Paredes M., Kraemer S. B., Mendoza C., 2014, MNRAS, 443, 1358
Mendoza C., 1983, in Aller L. H., ed., IAU Symposium Vol. 103, Planetary Nebulae. pp 143–172
Mignoli M., et al., 2019, A&A, 626, A9
Miller J. S., Mathews W. G., 1972, ApJ, 172, 593
Mingozzi M., et al., 2019, A&A, 622, A146
Mollá M., Díaz A. I., 2005, MNRAS, 358, 521
Moorwood A. F. M., Oliva E., 1988, A&A, 203, 278
Moorwood A. F. M., Salinari P., Furniss I., Jennings R. E., King K. J., 1980a, A&A, 90, 304
Moorwood A. F. M., Baluteau J. P., Anderegg M., Coron N., Biraud Y., Fitton B., 1980b, ApJ, 238, 565
Murdin P., 2003, Encyclopedia of Astronomy and Astrophysics. CRC Press
Nagao T., Murayama T., Shioya Y., Taniguchi Y., 2003, AJ, 125, 1729
Nagao T., Maiolino R., Marconi A., 2006, A&A, 459, 85
Nagao T., Maiolino R., Marconi A., Matsuhara H., 2011, A&A, 526, A149
Nakajima K., et al., 2018, A&A, 612, A94
Nieva M. F., Przybilla N., 2012, A&A, 539, A143

Nussbaumer H., Osterbrock D. E., 1970, ApJ, 161, 811
O'Donnell J. E., 1994, ApJ, 422, 158
Oliva E., Salvati M., Moorwood A. F. M., Marconi A., 1994, A&A, 288, 457
Onori F., et al., 2017, MNRAS, 464, 1783
Osterbrock D. E., 1989, Astrophysics of gaseous nebulae and active galactic nuclei. UNIVERSITY SCIENCE BOOKS
Osterbrock D. E., Dahari O., 1983, ApJ, 273, 478
Osterbrock D. E., Ferland G. J., 2006, Astrophysics of gaseous nebulae and active galactic nuclei. UNIVERSITY SCIENCE BOOKS
Osterbrock D. E., Miller J. S., 1975, ApJ, 197, 535
Osterbrock D. E., Tran H. D., Veilleux S., 1992, ApJ, 389, 305
Pagel B. E. J., Simonson E. A., Terlevich R. J., Edmunds M. G., 1992, MNRAS, 255, 325
Peimbert M., 1967, ApJ, 150, 825
Peimbert M., Costero R., 1969, Boletin de los Observatorios Tonantzintla y Tacubaya, 5, 3
Peimbert M., Peimbert A., 2009, arXiv e-prints, p. arXiv:0912.3781
Peimbert A., Peimbert M., 2010, ApJ, 724, 791
Peimbert M., Torres-Peimbert S., Ruiz M. T., 1992, Rev. Mex. Astron. Astrofis., 24, 155
Peimbert M., Torres-Peimbert S., Dufour R. J., 1993, ApJ, 418, 760
Peimbert M., Peimbert A., Delgado-Inglada G., 2017, PASP, 129, 082001
Pereira-Santaella M., Diamond-Stanic A. M., Alonso-Herrero A., Rieke G. H., 2010, ApJ, 725, 2270
Pereira-Santaella M., Rigopoulou D., Farrah D., Lebouteiller V., Li J., 2017, MNRAS, 470, 1218
Pérez-Montero E., 2017, PASP, 129, 043001
Pérez-Montero E., Hägele G. F., Contini T., Díaz Á. I., 2007, MNRAS, 381, 125
Pérez-Montero E., et al., 2013, A&A, 549, A25
Pérez-Montero E., Dors O. L., Vílchez J. M., García-Benito R., Cardaci M. V., Hägele G. F., 2019, MNRAS, 489, 2652
Petrosian V., 1970, ApJ, 159, 833
Phillips M. M., 1981, MNRAS, 197, 659
Phillips M. M., Charles P. A., Baldwin J. A., 1983, ApJ, 266, 485
Pilyugin L. S., 2000, A&A, 362, 325
Pilyugin L. S., 2001, A&A, 369, 594
Pilyugin L. S., Vílchez J. M., Contini T., 2004, A&A, 425, 849
Pilyugin L. S., Thuan T. X., Vílchez J. M., 2007, MNRAS, 376, 353
Privon G. C., Baum S. A., O'Dea C. P., Gallimore J., Noel-Storr J., Axon D. J., Robinson A., 2012, ApJ, 747, 46
Puglisi A., et al., 2017, ApJ, 838, L18
Radovich M., Rafanelli P., 1996, A&A, 306, 97
Ramos Almeida C., Pérez García A. M., Acosta-Pulido J. A., 2009, ApJ, 694, 1379
Reunanen J., Kotilainen J. K., Prieto M. A., 2002, MNRAS, 331, 154
Revalski M., Crenshaw D. M., Kraemer S. B., Fischer T. C., Schmitt H. R., Machuca C., 2018a, ApJ, 856, 46
Revalski M., et al., 2018b, ApJ, 867, 88
Revalski M., et al., 2021, ApJ, 910, 139
Riffel R., Rodríguez-Ardila A., Pastoriza M. G., 2006, A&A, 457, 61
Riffel R. A., Storchi-Bergmann T., Dors O. L., Winge C., 2009, MNRAS, 393, 783
Riffel R. A., et al., 2016, MNRAS, 461, 4192
Riffel R. A., Hekatelyne C., Freitas I. C., 2018, Publ. Astron. Soc. Australia, 35, 40
Riffel R. A., et al., 2021a, MNRAS, 501, L54
Riffel R. A., Dors O. L., Krabbe A. C., Esteban C., 2021b, MNRAS, 506, L11

Ritter C., Herwig F., Jones S., Pignatari M., Fryer C., Hirschi R., 2018, MNRAS, 480, 538

Rodríguez-Ardila A., Riffel R., Pastoriza M. G., 2005, MNRAS, 364, 1041

Rosolowsky E., Simon J. D., 2008, ApJ, 675, 1213

Rubin R. H., Simpson J. P., Erickson E. F., Haas M. R., 1988, ApJ, 327, 377

Rubin R. H., et al., 2008, MNRAS, 387, 45

Salim S., Narayanan D., 2020, ARA&A, 58, 529

Salpeter E. E., 1955, ApJ, 121, 161

Saraph H. E., Tully J. A., 1994, A&AS, 107, 29

Shaw R. A., Dufour R. J., 1995, PASP, 107, 896

Shields G. A., Oke J. B., 1975, PASP, 87, 879

Shields G. A., Ludwig R. R., Salviander S., 2010, ApJ, 721, 1835

Shuder J. M., 1980, ApJ, 240, 32

Shuder J. M., Osterbrock D. E., 1981, ApJ, 250, 55

Simpson J. P., 1975, A&A, 39, 43

Skillman E. D., Kennicutt Robert C. J., 1993, ApJ, 411, 655

Skillman E. D., Berg D. A., Pogge R. W., Moustakas J., Rogers N. S. J., Croxall K. V., 2020, ApJ, 894, 138

Sofia U. J., 2004, in Witt A. N., Clayton G. C., Draine B. T., eds, Astronomical Society of the Pacific Conference Series Vol. 309, Astrophysics of Dust. p. 393

Sofia U. J., Cardelli J. A., Savage B. D., 1994, ApJ, 430, 650

Sosa-Brito R. M., Tacconi-Garman L. E., Lehnert M. D., Gallimore J. F., 2001, ApJS, 136, 61

Stanghellini L., Magrini L., Villaver E., Galli D., 2010, A&A, 521, A3

Stasińska G., 1984, A&A, 135, 341

Sternberg A., Genzel R., Tacconi L., 1994, ApJ, 436, L131

Storchi-Bergmann T., Pastoriza M. G., 1990, PASP, 102, 1359

Storchi-Bergmann T., Schmitt H. R., Calzetti D., Kinney A. L., 1998, AJ, 115, 909

Storchi-Bergmann T., McGregor P. J., Riffel R. A., Simões Lopes R., Beck T., Dopita M., 2009, MNRAS, 394, 1148

Storey P. J., Hummer D. G., 1995, MNRAS, 272, 41

Storey P. J., Zeippen C. J., 2000, MNRAS, 312, 813

Sturm E., Lutz D., Verma A., Netzer H., Sternberg A., Moorwood A. F. M., Oliva E., Genzel R., 2002, A&A, 393, 821

Thomas A. D., et al., 2017, ApJS, 232, 11

Thomas A. D., Kewley L. J., Dopita M. A., Groves B. A., Hopkins A. M., Sutherland R. S., 2018a, ApJ, 861, L2

Thomas A. D., Kewley L. J., Dopita M. A., Groves B. A., Hopkins A. M., Sutherland R. S., 2018b, ApJ, 861, L2

Thomas A. D., Kewley L. J., Dopita M. A., Groves B. A., Hopkins A. M., Sutherland R. S., 2019, ApJ, 874, 100

Tody D., 1986, in Crawford D. L., ed., Society of Photo-Optical Instrumentation Engineers (SPIE) Conference Series Vol. 627, Instrumentation in astronomy VI. p. 733, doi:10.1117/12.968154

Tommasin S., Spinoglio L., Malkan M. A., Fazio G., 2010, ApJ, 709, 1257

Torres-Peimbert S., Peimbert M., 1977, Rev. Mex. Astron. Astrofis., 2, 181

Tsamis Y. G., Barlow M. J., Liu X. W., Danziger I. J., Storey P. J., 2003, MNRAS, 338, 687

Ulrich M. H., Comastri A., Komossa S., Crane P., 1999, A&A, 350, 816

Vaona L., Ciroi S., Di Mille F., Cracco V., La Mura G., Rafanelli P., 2012, MNRAS, 427, 1266

Veilleux S., Osterbrock D. E., 1987, ApJS, 63, 295

Veilleux S., Goodrich R. W., Hill G. J., 1997, ApJ, 477, 631

Veilleux S., Sanders D. B., Kim D. C., 1999, ApJ, 522, 139

Verma A., Lutz D., Sturm E., Sternberg A., Genzel R., Vacca W., 2003, A&A, 403, 829

Vermeij R., van der Hulst J. M., 2002, A&A, 391, 1081

Viegas-Aldrovandi S. M., Contini M., 1989, ApJ, 339, 689

Vila-Costas M. B., Edmunds M. G., 1992, MNRAS, 259, 121

Wang W., Liu X. W., 2008, MNRAS, 389, L33

Ward M. J., Blanco P. R., Wilson A. S., Nishida M., 1991, ApJ, 382, 115

Weaver K. A., et al., 2010, ApJ, 716, 1151

Whitford A. E., 1958, AJ, 63, 201

Willner S. P., Nelson-Patel K., 2002, ApJ, 568, 679

Winge C., Storchi-Bergmann T., Ward M. J., Wilson A. S., 2000, MNRAS, 316, 1

Woosley S. E., Weaver T. A., 1995, ApJS, 101, 181

Wright E. L., 2006, PASP, 118, 1711

Wu Y.-Z., Zhao Y.-H., Meng X.-M., 2011, ApJS, 195, 17

Wysota A., Gaskell C. M., 1988, Reddening of Narrow Line Regions. pp 79–82, doi:10.1007/3-540-19492-4_171

York D. G., et al., 2000, AJ, 120, 1579

Zinchenko I. A., Dors O. L., Hägele G. F., Cardaci M. V., Krabbe A. C., 2019, MNRAS, 483, 1901

van Loon J. T., Oliveira J. M., Gordon K. D., Sloan G. C., Engelbracht C. W., 2010, AJ, 139, 1553

van Zee L., Salzer J. J., Haynes M. P., O'Donoghue A. A., Balonek T. J., 1998a, AJ, 116, 2805

van Zee L., Salzer J. J., Haynes M. P., O'Donoghue A. A., Balonek T. J., 1998b, AJ, 116, 2805

van der Laan T. P. R., Schinnerer E., Böker T., Armus L., 2013, A&A, 560, A99

Table A1. Flux (in units of 10^{-14} erg cm^{-2} s^{-1}) of [Ne III]λ12.81μm, [Ne III]λ15.56μm, Paschen and Brackett series for selected Seyfert 2 nuclei. In last but one and last columns, the redshift (z) and the original works where the data were compiled are listed, respectively.

Object	[Ne III]λ12.81μm	[Ne III]λ15.56μm	Paδ λ10052 Å	Paγ λ10941 Å	Paβ λ12822 Å	Paα λ18756 Å	Br11 λ16811 Å	Brδ λ19451 Å	Brγ λ21661 Å	Brβ λ26259 Å	Brα λ40523 Å	Redshift (z)	Ref.
NGC 3081	12.62 ± 1.16	36.46 ± 1.25	—	—	5.46	—	—	—	—	—	1.12	0.00798	[1, 5, 6]
NGC 4388	79.74 ± 4.76	108.18 ± 1.56	—	—	8.09	—	—	—	1.13	—	3.22	0.00842	[1, 5, 7]
NGC 4507	33.73 ± 2.63	28.78 ± 0.63	—	—	—	—	—	—	—	—	3.65	0.01180	[1, 6]
NGC 5135	112.00 ± 0.00	58.00 ± 0.00	—	—	—	—	—	—	1.65 ± 0.5	—	7.9	0.01369	[4, 9, 28]
NGC 5643	38.00 ± 0.00	56.00 ± 0.00	—	—	3.5	—	—	—	—	4.0	2.92	0.00400	[2, 4, 6, 7, 10]
NGC 5728	30.44 ± 1.81	54.76 ± 0.51	0.545 ± 0.142	0.380 ± 0.105	0.737 ± 0.116	2.063 ± 0.192	—	—	0.211 ± 0.019	—	—	0.00935	[1, 11]
IC 5063	28.22 ± 3.34	73.67 ± 4.61	—	—	—	—	—	—	1.00 ± 0.03	< 5.0	—	0.01135	[1, 6, 17]
IC 5135	71.00 ± 5.00	37.00 ± 2.00	—	—	—	—	—	—	1.02 ± 0.08	—	8.3	0.01615	[5, 9, 16, 28]
MRK 3	86.00 ± 12.00	207.00 ± 29.00	—	—	11.5	—	—	—	6.20 ± 0.40	—	—	0.01351	[5, 16, 25]
MRK 273	44.49 ± 0.79	33.81 ± 0.25	—	—	—	8.84	—	0.70	0.73 ± 0.04	4.2	4.4	0.03778	[8, 9, 12, 29]
MRK 348	15.34 ± 0.74	20.60 ± 0.79	0.27 ± 0.04	0.71 ± 0.12	1.21 ± 0.06	3.55 ± 0.15	—	0.33 ± 0.13	0.301 ± 0.042	—	—	0.01503	[1, 14]
MRK 573	13.00 ± 0.00	24.0 ± 0.00	0.327 ± 0.016	0.611 ± 0.04	0.958 ± 0.017	4.557 ± 0.028	—	0.137 ± 0.006	0.277 ± 0.009	—	—	0.01718	[10, 11]
NGC 1068	538.34 ± 37.3	1432.20 ± 76.87	—	—	—	—	—	—	12.7	41.0	69.0	0.00379	[5, 10, 12, 15]
NGC 2992	53.65 ± 3.66	61.06 ± 1.98	2.65	3.7	5.1	8.8	0.56	—	1.16	—	6.65	0.00771	[1, 6, 19]
NGC 5506	91.75 ± 3.31	152.13 ± 9.13	—	—	85.1	—	—	—	11.8	7.0	12.0	0.00618	[1, 5, 10]
NGC 7674	18.00 ± 1.00	46.00 ± 2.00	0.838 ± 0.067	1.387 ± 0.131	1.036 ± 0.058	3.206 ± 1.009	2.566 ± 0.452	0.338 ± 0.051	0.313 ± 0.025	—	—	0.02892	[11, 16]
I Zw 92	24.00 ± 0.00	16.00 ± 0.00	—	—	10.4	—	—	—	0.953	—	—	0.03780	[5, 10]
NGC 2110	60.19 ± 5.34	47.40 ± 0.71	0.300 ± 0.027	1.266 ± 0.103	1.491 ± 0.086	3.295 ± 0.450	—	—	0.250 ± 0.022	—	2.11	0.00779	[1, 6, 11]
NGC 5929	13.20 ± 0.34	9.83 ± 0.31	—	0.379 ± 0.027	0.768 ± 0.020	—	—	—	0.135 ± 0.025	—	—	0.00831	[11, 13]
MRK 463E	10.82 ± 0.35	40.46 ± 0.73	—	—	3.01	—	—	—	0.272	4.0	—	0.05035	[5, 8]
MRK 622	6.00 ± 2.00	8.00 ± 2.00	—	—	1.02	—	—	—	—	—	—	0.02323	[5, 16]
NGC 1386	17.8 ± 1.02	36.6 ± 0.72	—	—	3.50	—	—	—	0.176 ± 0.014	—	—	0.00290	[2, 3, 13]
NGC 7582	250.94 ± 3.53	105.00 ± 2.05	—	—	7.8	—	—	—	4.4 ± 0.4	9.0	20.6 ± 7.0	0.00525	[2, 10, 13, 18]
NGC 1275	46.15 ± 0.80	22.37 ± 0.56	1.332 ± 0.108	8.353 ± 0.425	6.066 ± 0.315	14.514 ± 0.252	—	1.398 ± 0.206	0.977 ± 0.041	2	22	0.01756	[8, 10, 11]
Circinus	453.6 ± 14.5	400.00 ± 9.00	—	10.4	—	—	—	—	3.8	32	15.0	0.00145	[8, 10, 20]
Centaurus A	221.00 ± 4.50	140.00 ± 1.20	—	19	16	—	—	—	2.7	9.0	8.0	0.00183	[3, 8, 10, 26]
Cygnus A	26.7 ± 0.3	41.30 ± 0.40	—	—	—	2.6 ± 0.2	—	—	0.26 ± 0.08	—	—	0.05607	[21, 22]
MRK 266SW	57.00 ± 0.00	28.00 ± 0.00	—		5.51	—	—	—	0.367	—	4.5	0.02760	[4, 5, 9]
MRK 1066	10.94 ± 0.21	46.91 ± 0.76	0.974 ± 0.030	2.553 ± 0.120	5.407 ± 0.024	14.574 ± 1.060	0.398 ± 0.055	0.867 ± 0.004	1.416 ± 0.022	—	—	0.01202	[8, 11]
NGC 1320	—	9.00 ± 1.00	—	—	—	—	—	—	0.094 ± 0.01	—	—	0.00888	[16, 25]
NGC 1667	10.1 ± 3.00	7.23 ± 3.00	—	—	—	—	—	—	0.018 ± 0.004	—	—	0.01517	[16, 25]
NGC 3393	—	95.00 ± 0.00	—	—	—	—	—	—	0.46 ± 0.005	—	—	0.01251	[24, 27]
NGC 5953	105.00 ± 2.00	21.00 ± 1.00	—	—	0.544	1.982 ± 0.083	—	—	0.277	—	—	0.00656	[11, 16, 23]
NGC 7682	5.46 ± 0.25	8.07 ± 0.15	0.118 ± 0.018	0.498 ± 0.112	0.992 ± 0.065	3.182 ± 0.081	—	—	0.194 ± 0.011	—	—	0.01714	[1, 11]
ESO428 − G014	—	168.01 ± 0.00	0.919 ± 0.063	3.104 ± 0.115	4.526 ± 0.057	10.205 ± 0.078	0.822 ± 0.029	0.300 ± 0.049	0.898 ± 0.014	—	—	0.00566	[11, 24]

References: (1) Weaver et al. (2010), (2) Winge et al. (2000), (3) Reunanen et al. (2002), (4) Pereira-Santaella et al. (2010), (5) Veilleux et al. (1997), (6) Lutz et al. (2002), (7) Onori et al. (2017), (8) Dasyra et al. (2011), (9) Imanishi et al. (2010), (10) Sturm et al. (2002), (11) Riffel et al. (2006), (12) Goldader et al. (1995), (13) Tommasin et al. (2010), (14) Ramos Almeida et al. (2009), (15) Goulding & Alexander (2009), (16) Deo et al. (2007), (17) Moorwood & Oliva (1988), (18) Kawara et al. (1989), (19) Gilli et al. (2000), (20) Oliva et al. (1994), (21) Privon et al. (2012), (22) Ward et al. (1991), (23) Rodríguez-Ardila et al. (2005), (24) Wu et al. (2011), (25) van der Laan et al. (2013), (26) Bryant & Hunstead (1999), (27) Sosa-Brito et al. (2001), (28) Goldader et al. (1997) and (29) Veilleux et al. (1999).

Table A2. Observed reddening-uncorrected optical emission-line intensities of Seyfert 2 nuclei compiled from the literature. The last column is the list of references for the original works where the data were obtained.

Object	[O II] λ3727 Å	[Ne III] λ3869 Å	[O III] λ4363 Å	[O III] λ4959 Å	[O III] λ5007 Å	[O I] λ6300 Å	Hα λ6563 Å	Hβ λ4861 Å	[N II] λ6584 Å	[S II] λ6717 Å	[S II] λ6731 Å	Ref.
NGC 3081	1.47	0.88	0.20	4.53	13.30	0.37	4.53	1.00	3.87	0.99	1.07	1
NGC 4388	1.72	0.48	0.13	3.83	11.20	0.78	4.86	1.00	2.59	1.27	1.12	1
NGC 4507	1.64	0.71	0.27	3.17	9.53	0.86	5.16	1.00	2.80	1.10	1.23	1
NGC 5135	1.06	0.42	0.08	1.49	4.82	0.31	6.12	1.00	5.45	0.92	0.87	1
NGC 5643	2.68	0.89	0.32	4.85	16.60	1.16	6.17	1.00	7.17	2.40	2.21	1
NGC 5728	1.84	0.75	0.34	3.92	11.80	1.00	5.97	1.00	8.36	0.99	0.97	1
IC 5063	2.90	0.75	0.22	3.55	11.00	0.68	5.55	1.00	3.44	1.50	1.31	1
IC 5135	2.15	1.04	0.19	2.20	7.41	0.60	6.07	1.00	7.56	1.19	1.11	1
MRK 3	2.21	0.94	0.19	4.16	13.46	1.14	5.31	1.00	5.48	1.30	1.46	2
MRK 273	3.05	0.71	0.13	5.39	17.96	1.22	28.20	3.06	29.30	17.50	5.15	2, 3
MRK 348	3.05	1.23	0.21	3.96	12.33	1.58	4.27	1.00	3.54	1.74	2.01	2
MRK 573	2.11	1.01	0.15	4.01	12.64	0.43	4.30	1.00	3.62	1.12	1.21	2
NGC 1068	0.76	0.94	0.17	4.28	13.22	0.62	4.47	1.00	7.94	0.48	0.99	2
NGC 2992	0.19	0.04	0.01	0.32	1.00	0.15	1.73	0.13	1.00	0.46	0.41	4
NGC 5506	0.14	0.04	0.01	0.31	1.00	0.11	0.87	0.12	0.80	0.32	0.34	4
NGC 7674	1.08	0.98	0.11	3.99	12.82	0.38	4.62	1.00	4.62	0.69	0.81	5
I Zw 92	1.95	0.94	0.28	3.60	10.50	0.55	3.54	1.00	1.43	0.55	0.60	5
NGC 2110ᵃ	21.10	4.20	0.73	11.17	33.50	8.20	18.00	4.30	34.00	7.90	9.80	6
NGC 5929ᵃ	14.80	2.21	0.40	4.23	12.70	8.20	20.60	4.40	12.10	7.60	6.70	6
MRK 463E	0.21	0.07	0.013	0.33	1.00	0.055	0.48	0.13	0.23	0.10	0.09	7
MRK 622	0.49	0.06	0.004	0.33	1.00	0.041	1.88	0.16	1.77	0.32	0.35	7
NGC 1386ᵃ	1.81	0.77	0.19	3.78	11.34	0.46	4.70	1.00	5.60	1.04	1.29	8
NGC 7582	124.10	32.80	2.90	71.60	214.70	8.70	286.00	100.00	186.90	41.80	38.80	9
NGC 1275	2.90	1.43	0.33	4.33	12.99	1.48	5.44	1.00	5.44	1.33	4.52	10
Circinus	78.00	41.00	16.00	317.00	1048.00	46.00	565.00	100.00	154.00	128.00	113.00	11
Centaurus A	2.49	0.48	0.10	2.38	6.28	2.05	7.27	1.00	10.83	5.24	4.17	12
Cygnus A	2.44	0.66	0.16	4.08	13.11	2.10	6.61	1.00	13.07	3.65	3.29	13
MRK 266SW	5.20	0.90	0.08	1.50	4.50	0.38	3.30	1.00	3.68	0.54	0.46	14
MRK 1066	0.32	0.08	0.01	0.31	1.00	0.15	1.80	0.23	1.58	0.36	0.39	15
NGC 1320	0.38	0.49	0.29	3.57	9.86	0.38	4.86	1.00	3.36	0.93	1.07	16, 17
NGC 1667	12.08	1.98	0.42	3.99	11.10	0.94	3.03	1.00	6.59	2.86	9.72	18, 19
NGC 3393	155.00	77.00	10.00	341.00	1030.00	34.00	359.00	100.00	492.00	202.00	686.80	20
NGC 5953	2.60	0.90	0.12	1.70	4.30	0.32	2.90	1.00	4.00	0.80	0.84	21
NGC 7682ᵃ	575.00	158.00	77.40	1310.00	3930.00	167.00	470.00	100.00	515.00	134.00	141.00	22
ESO 428 − G014	2.49	1.13	0.28	4.20	13.60	0.49	3.55	1.00	4.03	1.07	1.14	23

References: (1) Phillips et al. (1983), (2) Koski (1978), (3) Malkan et al. (2017), (4) Shuder (1980), (5) Kraemer et al. (1994), (6) Ferruit et al. (1999), (7) Shuder & Osterbrock (1981), (8) Bennert et al. (2006), (9) Dopita et al. (2015), (10) Shields & Oke (1975), (11) Oliva et al. (1994), (12) Phillips (1981), (13) Osterbrock & Miller (1975), (14) Osterbrock & Dahari (1983), (15) Goodrich & Osterbrock (1983), (16) De Robertis & Osterbrock (1986), (17) Thomas et al. (2017), (18) Ho et al. (1993), (19) Radovich & Rafanelli (1996), (20) Cooke et al. (2000), (21) Gonzalez Delgado & Perez (1996), (22) Durret (1994) and (23) Bergvall et al. (1986).
Note: ᵃValue of $I($[O III]$\lambda4959)$ estimated from the theoretical relation I[O III]$\lambda4959 = I$[O III]$\lambda5007/3.0$ (Storey & Zeippen 2000).

Table A3. Reddening-corrected optical emission-line intensities (relative to Hβ=1.0) of Seyfert 2 nuclei compiled from the literature. Original works which the data were obtained are presented in Table A2.

Object	[O II] λ3727 Å	[Ne III] λ3869 Å	[O III] λ4363 Å	[O III] λ4959 Å	[O III] λ5007 Å	[O I] λ6300 Å	Hα λ6563 Å	[N II] λ6584 Å	[S II] λ6717 Å	[S II] λ6731 Å	c(Hβ)
f(λ)	0.302	0.260	0.125	− 0.022	− 0.033	− 0.285	− 0.326	− 0.329	− 0.349	− 0.350	
NGC 3081	2.26	1.28	0.24	4.39	12.69	0.25	2.85	2.42	0.60	0.65	0.6192
NGC 4388	2.82	0.74	0.16	3.70	10.61	0.49	2.84	1.51	0.72	0.63	0.7139
NGC 4507	2.85	1.14	0.34	3.05	8.97	0.51	2.84	1.53	0.58	0.65	0.7946
NGC 5135	2.16	0.78	0.11	1.42	4.46	0.16	2.84	2.51	0.40	0.38	1.0243
NGC 5643	5.50	1.66	0.43	4.60	15.35	0.59	2.83	3.27	1.05	0.96	1.0352
NGC 5728	3.66	1.36	0.45	3.73	10.95	0.52	2.84	3.94	0.45	0.44	0.9909
IC 5063	5.39	1.28	0.28	3.39	10.28	0.38	2.84	1.75	0.73	0.64	0.8927
IC 5135	4.35	1.91	0.25	2.09	6.86	0.31	2.84	3.51	0.53	0.49	1.0132
MRK 3	3.94	1.55	0.24	3.99	12.64	0.66	2.84	2.91	0.67	0.75	0.8331
MRK 273	2.98	0.60	0.07	1.63	5.21	0.14	2.82	2.90	1.62	0.47	1.5755
MRK 348	4.44	1.70	0.25	3.85	11.84	1.11	2.85	2.35	1.13	1.30	0.5396
MRK 573	3.09	1.40	0.18	3.90	12.13	0.30	2.85	2.39	0.72	0.78	0.5491
NGC 1068	1.15	1.35	0.20	4.15	12.63	0.42	2.85	5.03	0.30	0.61	0.6013
NGC 2992	6.16	1.17	0.18	2.22	6.58	0.30	2.81	1.60	0.67	0.59	2.0702
NGC 5506	2.78	0.69	0.13	2.43	7.58	0.40	2.83	2.58	0.98	1.03	1.2524
NGC 7674	1.69	1.44	0.13	3.86	12.21	0.25	2.84	2.83	0.41	0.48	0.6457
I Zw 92	2.38	1.12	0.30	3.55	10.27	0.46	2.85	1.15	0.44	0.48	0.2872
NGC 2110	7.01	1.33	0.20	2.53	7.49	1.36	2.85	5.36	1.22	1.51	0.5129
NGC 5929	5.33	0.75	0.11	0.93	2.75	1.21	2.84	1.66	1.01	0.89	0.6636
MRK 463E	2.05	0.61	0.11	2.50	7.49	0.34	2.85	2.30	0.57	0.52	0.3439
MRK 622	11.48	1.25	0.04	1.87	5.41	0.07	2.81	2.61	0.43	0.47	1.9026
NGC 1386	2.88	1.15	0.23	3.66	10.78	0.30	2.84	3.37	0.61	0.75	0.6688
NGC 7582	1.24	0.33	0.03	0.72	2.15	0.09	2.86	1.87	0.42	0.39	0.0000
NGC 1275	5.29	2.40	0.42	4.15	12.17	0.84	2.84	2.82	0.66	2.25	0.8657
Circinus	1.47	0.71	0.21	3.03	9.78	0.25	2.84	0.77	0.61	0.54	0.9167
Centaurus A	5.96	1.02	0.14	2.23	5.71	0.90	2.83	4.18	1.91	1.51	1.2561
Cygnus A	5.34	1.30	0.22	3.86	12.04	1.00	2.83	5.56	1.48	1.32	1.1280
MRK 266SW	5.94	1.01	0.08	1.49	4.43	0.33	2.86	3.18	0.46	0.39	0.1927
MRK 1066	3.57	0.74	0.08	1.26	3.92	0.27	2.83	2.46	0.53	0.57	1.3554
NGC 1320	0.62	0.74	0.36	3.44	9.34	0.24	2.84	1.96	0.52	0.60	0.7139
NGC 1667	12.75	2.07	0.43	3.97	11.03	0.89	2.86	6.21	2.69	9.13	0.0777
NGC 3393	1.92	0.93	0.11	3.36	10.06	0.28	2.85	3.90	1.58	5.36	0.3061
NGC 5953	2.63	0.91	0.12	1.70	4.29	0.32	2.86	3.94	0.79	0.83	0.0187
NGC 7682	9.15	2.36	0.94	12.67	37.36	1.08	2.84	3.10	0.78	0.82	0.6688
ESO428 − G014	3.05	1.13	0.30	4.14	13.30	0.40	2.85	3.23	0.85	0.90	0.2910

Table A4. Ionic and total neon abundances for the Seyfert 2 sample obtained through IR-method using the methodology described in Sect. 4.2. The abundances $12 + \log(\mathrm{Ne^+/H^+})$ and $12 + \log(\mathrm{Ne^{2+}/H^{2+}})$ are calculated by using the Eqs. 17 to 20. The term f represents the correction for the total neon abundance $12 + \log(\mathrm{Ne/H})$ due to the presence of ions with ionization stages higher than $\mathrm{Ne^{2+}}$ (see Eq. 31) which is derived from photoionization models by Carvalho et al. (2020).

Object	$12 + \log(\mathrm{Ne^+/H^+})_{\mathrm{IR}}$	$12 + \log(\mathrm{Ne^{2+}/H^+})_{\mathrm{IR}}$	f	$12 + \log(\mathrm{Ne/H})_{\mathrm{IR}}$
NGC 3081	8.05 ± 0.07	8.19 ± 0.07	1.13	8.48 ± 0.07
NGC 4388	8.40 ± 0.06	8.21 ± 0.06	1.11	8.64 ± 0.06
NGC 4507	7.99 ± 0.09	7.60 ± 0.09	1.03	8.15 ± 0.09
NGC 5135	8.29 ± 0.10	7.68 ± 0.10	1.03	8.40 ± 0.08
NGC 5643	8.35 ± 0.11	8.20 ± 0.12	1.03	8.60 ± 0.09
NGC 5728	8.84 ± 0.03	8.88 ± 0.01	1.04	9.18 ± 0.01
IC 5063	7.84 ± 0.03	7.93 ± 0.03	1.03	8.25 ± 0.03
IC 5135	8.24 ± 0.03	7.63 ± 0.03	1.04	8.35 ± 0.03
MRK 3	8.03 ± 0.07	8.09 ± 0.07	1.06	8.39 ± 0.07
MRK 273	8.19 ± 0.04	7.75 ± 0.04	1.04	8.35 ± 0.04
MRK 348	8.38 ± 0.03	8.19 ± 0.03	1.04	8.62 ± 0.03
MRK 573	8.35 ± 0.09	8.29 ± 0.09	1.11	8.67 ± 0.06
NGC 1068	8.03 ± 0.06	8.14 ± 0.06	1.32	8.51 ± 0.06
NGC 2992	8.18 ± 0.03	7.92 ± 0.03	1.04	8.39 ± 0.03
NGC 5506	7.73 ± 0.05	7.63 ± 0.05	1.06	8.01 ± 0.05
NGC 7674	8.33 ± 0.03	8.41 ± 0.02	1.27	8.78 ± 0.02
IZw 92	7.85 ± 0.12	7.36 ± 0.12	1.04	7.99 ± 0.10
NGC 2110	8.91 ± 0.01	8.49 ± 0.01	1.04	9.07 ± 0.01
NGC 5929	8.58 ± 0.03	8.14 ± 0.03	1.06	8.74 ± 0.03
MRK 463E	7.91 ± 0.07	8.16 ± 0.07	1.10	8.40 ± 0.07
MRK 622	8.11 ± 0.10	7.91 ± 0.09	1.03	8.33 ± 0.09
NGC 1386	8.38 ± 0.02	8.37 ± 0.02	1.06	8.70 ± 0.02
NGC 7582	8.48 ± 0.06	7.78 ± 0.06	1.04	8.58 ± 0.06
NGC 1275	8.19 ± 0.02	7.56 ± 0.02	1.03	8.29 ± 0.02
Circinus	8.54 ± 0.05	8.17 ± 0.05	1.13	8.75 ± 0.05
Centaurus A	8.38 ± 0.05	7.87 ± 0.05	1.04	8.52 ± 0.05
Cygnus A	8.62 ± 0.02	8.49 ± 0.02	1.04	8.87 ± 0.02
MRK 266SW	8.49 ± 0.11	7.86 ± 0.11	1.04	8.60 ± 0.10
MRK 1066	7.62 ± 0.01	8.00 ± 0.01	1.03	8.16 ± 0.01
NGC 1320	—	8.22 ± 0.07	1.09	—
NGC 1667	9.32 ± 0.11	8.86 ± 0.11	1.05	9.47 ± 0.11
NGC 3393	—	8.55 ± 0.09	1.20	—
NGC 5953	9.43 ± 0.05	8.41 ± 0.05	1.03	9.48 ± 0.05
NGC 7682	8.19 ± 0.04	8.04 ± 0.03	1.05	8.44 ± 0.03
ESO428−G014	—	8.58 ± 0.09	1.07	—

Table A5. Estimates of Ne ionic and total abundances based on the electron temperatures t_3 and $t_{\mathrm{e}}(\mathrm{Ne\,III})$ for the Seyfert 2 sample.

Object	$12 + \log(\mathrm{Ne^{2+}/H^+})_{t_3}$	$12 + \log(\mathrm{Ne^{2+}/H^+})_{t_{\mathrm{e}}(\mathrm{Ne\,III})}$	$\mathrm{ICF(Ne^{2+})}$	$12 + \log(\mathrm{Ne/H})_{t_3}$	$12 + \log(\mathrm{Ne/H})_{t_{\mathrm{e}}(\mathrm{Ne\,III})}$
NGC 3081	7.57 ± 0.14	7.99 ± 0.07	1.93	7.85 ± 0.14	8.28 ± 0.07
NGC 4388	7.46 ± 0.14	7.81 ± 0.08	2.81	7.91 ± 0.14	8.26 ± 0.08
NGC 4507	7.10 ± 0.14	7.80 ± 0.08	3.55	7.65 ± 0.14	8.34 ± 0.08
NGC 5135	7.18 ± 0.14	7.71 ± 0.06	5.19	7.90 ± 0.14	8.43 ± 0.06
NGC 5643	7.43 ± 0.14	8.02 ± 0.06	2.48	7.82 ± 0.14	8.41 ± 0.06
NGC 5728	7.13 ± 0.14	7.84 ± 0.10	2.24	7.48 ± 0.14	8.19 ± 0.10
IC 5063	7.34 ± 0.13	7.91 ± 0.06	1.84	7.61 ± 0.13	8.18 ± 0.06
IC 5135	7.34 ± 0.14	8.02 ± 0.08	5.21	8.05 ± 0.14	8.74 ± 0.08
MRK 3	7.63 ± 0.14	8.07 ± 0.07	1.97	7.93 ± 0.14	8.36 ± 0.07
MRK 273	7.42 ± 0.13	7.75 ± 0.08	3.90	8.01 ± 0.13	8.34 ± 0.08
MRK 348	7.61 ± 0.14	8.09 ± 0.07	2.65	8.04 ± 0.14	8.51 ± 0.07
MRK 573	7.73 ± 0.13	8.09 ± 0.08	2.35	8.11 ± 0.13	8.46 ± 0.08
NGC 1068	7.69 ± 0.14	8.06 ± 0.08	2.34	8.06 ± 0.14	8.43 ± 0.08
NGC 2992	7.30 ± 0.14	7.87 ± 0.06	2.94	7.77 ± 0.14	8.34 ± 0.06
NGC 5506	7.35 ± 0.14	7.74 ± 0.07	2.38	7.72 ± 0.14	8.12 ± 0.07
NGC 7674	7.93 ± 0.13	8.20 ± 0.09	2.29	8.29 ± 0.13	8.56 ± 0.09
IZw 92	7.25 ± 0.14	7.84 ± 0.06	4.30	7.88 ± 0.14	8.48 ± 0.06
NGC 2110	7.37 ± 0.14	7.93 ± 0.06	3.79	7.96 ± 0.14	8.51 ± 0.06
NGC 5929	6.89 ± 0.14	7.60 ± 0.09	4.03	7.49 ± 0.14	8.20 ± 0.09
Mrk 463E	7.39 ± 0.14	7.73 ± 0.08	1.70	7.62 ± 0.14	7.96 ± 0.08
Mrk 622	8.07 ± 0.12	8.28 ± 0.10	2.63	8.49 ± 0.12	8.70 ± 0.10
NGC 1386	7.45 ± 0.14	7.92 ± 0.07	2.12	7.78 ± 0.14	8.24 ± 0.07
NGC 7582	7.15 ± 0.13	7.48 ± 0.08	6.24	7.94 ± 0.13	8.27 ± 0.08
NGC 1275	7.48 ± 0.14	8.14 ± 0.07	5.47	8.22 ± 0.14	8.88 ± 0.07
Circinus	7.22 ± 0.14	7.70 ± 0.07	3.80	7.80 ± 0.14	8.28 ± 0.07
Centaurus A	7.33 ± 0.14	7.84 ± 0.06	4.47	7.98 ± 0.14	8.49 ± 0.06
Cygnus A	7.59 ± 0.14	8.00 ± 0.07	2.43	7.97 ± 0.14	8.39 ± 0.07
Mrk 266SW	7.48 ± 0.12	7.90 ± 0.07	5.47	8.22 ± 0.12	8.63 ± 0.07
Mrk 1066	7.27 ± 0.14	7.73 ± 0.07	1.52	7.46 ± 0.14	7.91 ± 0.07
NGC 1320	6.92 ± 0.14	7.61 ± 0.08	—	—	—
NGC 1667	7.35 ± 0.14	8.05 ± 0.08	4.11	7.97 ± 0.14	8.66 ± 0.08
NGC 3393	7.73 ± 0.13	8.01 ± 0.09	—	—	—
NGC 5953	7.21 ± 0.14	7.77 ± 0.06	11.83	8.28 ± 0.14	8.84 ± 0.06
NGC 7682	7.66 ± 0.14	8.19 ± 0.06	2.52	8.06 ± 0.14	8.60 ± 0.06
ESO428−G014	7.39 ± 0.14	7.89 ± 0.07	—	—	—

Table A6. Estimates for the Seyfert 2 sample of electron temperature t_3 (in units of 10^4 K), ionic and total oxygen abundances, ionization correction factor (ICF) for the oxygen, and the logarithm of Ne/O assuming t_3 and $t_3(\text{Ne\,III})$ in the Ne derivations.

Object	t_3	$12 + \log(O^+/H^+)$	$12 + \log(O^{2+}/H^+)$	ICF(O)	$12 + \log(O/H)$	$\log(\text{Ne/O})_{t_3}$	$\log(\text{Ne/O})_{t_3(\text{Ne\,III})}$
NGC 3081	1.48 ± 0.15	8.06 ± 0.05	8.14 ± 0.13	1.45 ± 0.07	8.57 ± 0.08	-0.71 ± 0.08	-0.29 ± 0.06
NGC 4388	1.34 ± 0.12	8.17 ± 0.06	8.17 ± 0.12	1.21 ± 0.03	8.56 ± 0.08	-0.65 ± 0.07	-0.30 ± 0.05
NGC 4507	2.18 ± 0.29	8.33 ± 0.11	7.62 ± 0.13	1.00	8.41 ± 0.07	-0.76 ± 0.19	-0.07 ± 0.13
NGC 5135	1.71 ± 0.20	8.06 ± 0.06	7.53 ± 0.13	1.22 ± 0.03	8.27 ± 0.05	-0.28 ± 0.15	$+0.25 \pm 0.07$
NGC 5643	1.85 ± 0.23	8.51 ± 0.08	7.98 ± 0.13	1.00	8.63 ± 0.05	-0.81 ± 0.16	-0.22 ± 0.09
NGC 5728	2.29 ± 0.32	8.46 ± 0.11	7.67 ± 0.13	1.22 ± 0.03	8.63 ± 0.08	-1.06 ± 0.19	-0.34 ± 0.14
IC 5063	1.80 ± 0.20	8.48 ± 0.07	7.85 ± 0.13	1.15 ± 0.02	8.64 ± 0.05	-0.97 ± 0.15	-0.40 ± 0.08
IC 5135	2.16 ± 0.29	8.50 ± 0.11	7.50 ± 0.13	1.41 ± 0.06	8.70 ± 0.09	-0.50 ± 0.21	$+0.19 \pm 0.14$
MRK 3	1.50 ± 0.15	8.31 ± 0.05	8.11 ± 0.13	1.25 ± 0.04	8.62 ± 0.06	-0.59 ± 0.10	-0.16 ± 0.05
MRK 273	1.29 ± 0.11	8.21 ± 0.06	7.89 ± 0.12	2.24 ± 0.18	8.73 ± 0.08	-0.37 ± 0.08	-0.05 ± 0.05
MRK 348	1.58 ± 0.17	8.35 ± 0.05	8.03 ± 0.13	1.19 ± 0.03	8.61 ± 0.06	-0.49 ± 0.11	-0.02 ± 0.06
MRK 573	1.34 ± 0.12	8.21 ± 0.06	8.22 ± 0.12	1.40 ± 0.06	8.67 ± 0.09	-0.41 ± 0.07	-0.06 ± 0.05
NGC 1068	1.38 ± 0.13	7.78 ± 0.06	8.21 ± 0.13	1.28 ± 0.04	8.43 ± 0.08	-0.29 ± 0.06	$+0.08 \pm 0.06$
NGC 2992	1.80 ± 0.22	8.54 ± 0.07	7.65 ± 0.13	1.20 ± 0.03	8.68 ± 0.06	-0.82 ± 0.18	-0.25 ± 0.10
NGC 5506	1.43 ± 0.14	8.15 ± 0.05	7.94 ± 0.13	1.19 ± 0.03	8.44 ± 0.07	-0.64 ± 0.09	-0.25 ± 0.05
NGC 7674	1.18 ± 0.09	8.01 ± 0.07	8.37 ± 0.12	1.24 ± 0.04	8.63 ± 0.10	-0.24 ± 0.06	$+0.03 \pm 0.05$
IZw 92	1.86 ± 0.23	8.14 ± 0.08	7.82 ± 0.13	1.19 ± 0.03	8.40 ± 0.05	-0.44 ± 0.15	$+0.16 \pm 0.07$
NGC 2110	1.77 ± 0.21	8.59 ± 0.07	7.72 ± 0.13	1.00	8.65 ± 0.06	-0.69 ± 0.17	-0.13 ± 0.09
NGC 5929	2.25 ± 0.31	8.62 ± 0.11	7.08 ± 0.13	1.08 ± 0.01	8.67 ± 0.10	-1.14 ± 0.22	-0.43 ± 0.16
Mrk 463E	1.33 ± 0.12	8.04 ± 0.06	8.02 ± 0.12	1.13 ± 0.02	8.39 ± 0.08	-0.71 ± 0.07	-0.37 ± 0.05
Mrk 622	1.04 ± 0.07	8.95 ± 0.08	8.20 ± 0.11	1.46 ± 0.07	9.18 ± 0.09	-0.53 ± 0.07	-0.32 ± 0.06
NGC 1386	1.57 ± 0.17	8.17 ± 0.05	8.00 ± 0.13	1.00	8.40 ± 0.06	-0.62 ± 0.10	-0.16 ± 0.05
NGC 7582	1.31 ± 0.12	7.83 ± 0.06	7.50 ± 0.12	1.11 ± 0.02	8.04 ± 0.07	-0.05 ± 0.08	$+0.28 \pm 0.06$
NGC 1275	2.05 ± 0.27	8.55 ± 0.10	7.81 ± 0.13	1.27 ± 0.04	8.74 ± 0.07	-0.41 ± 0.20	$+0.25 \pm 0.12$
Circinus	1.60 ± 0.17	7.88 ± 0.05	7.93 ± 0.13	1.65 ± 0.09	8.43 ± 0.07	-0.41 ± 0.09	$+0.07 \pm 0.05$
Centaurus A	1.66 ± 0.19	8.49 ± 0.06	7.69 ± 0.13	1.11 ± 0.02	8.61 ± 0.05	-0.58 ± 0.15	-0.07 ± 0.08
Cygnus A	1.47 ± 0.15	8.43 ± 0.05	8.11 ± 0.13	1.45 ± 0.06	8.77 ± 0.06	-0.64 ± 0.10	-0.22 ± 0.06
Mrk 266SW	1.46 ± 0.13	8.48 ± 0.05	7.69 ± 0.13	1.23 ± 0.03	8.64 ± 0.05	-0.32 ± 0.11	$+0.08 \pm 0.07$
Mrk 1066	1.55 ± 0.17	8.26 ± 0.05	7.57 ± 0.13	1.22 ± 0.03	8.43 ± 0.05	-0.89 ± 0.13	-0.43 ± 0.07
NGC 1320	2.17 ± 0.29	7.66 ± 0.11	7.65 ± 0.13	1.41 ± 0.06	8.12 ± 0.05	—	—
NGC 1667	2.19 ± 0.30	8.98 ± 0.11	7.72 ± 0.13	1.00	9.01 ± 0.09	-1.04 ± 0.22	-0.34 ± 0.15
NGC 3393	1.19 ± 0.09	8.06 ± 0.07	8.29 ± 0.12	1.00	8.49 ± 0.10	—	—
NGC 5953	1.78 ± 0.21	8.16 ± 0.07	7.50 ± 0.13	1.00	8.25 ± 0.05	$+0.03 \pm 0.16$	$+0.59 \pm 0.08$
NGC 7682	1.72 ± 0.20	8.69 ± 0.06	8.45 ± 0.13	1.00	8.90 ± 0.05	-0.84 ± 0.12	-0.30 ± 0.06
ESO428−G014	1.64 ± 0.18	8.20 ± 0.06	8.04 ± 0.13	1.16 ± 0.02	8.50 ± 0.06	—	—

Note: ICF(O) is assumed to be equal to 1.00 where the He I $\lambda 5846$ Å emission line was not presented in the original work.